

MASTER'S THESIS
TRABAJO DE FIN DE MASTER

The impact of flares on
prominences in the Sun

Óscar Soler Pérez

Supervisors

Fernando Moreno Insertis
Manuel Luna Bennasar



University of La Laguna
Master's Degree in Astrophysics

June, 2025

Acknowledgements

I would like to express my deepest gratitude to my supervisors, Fernando Moreno Insertis and Manuel Luna Bennasar, for making this work possible. Thank you for guiding me along the path of knowledge, for revealing to me the beauty of solar physics, and for your unwavering support in the face of every challenge encountered.

My gratitude also extends to all those who believed in me and stood by my side throughout these months of hard work. To my parents for their unconditional support. To my friends, thank you for inspiring me to always give my best.

The author thankfully acknowledges the technical expertise and assistance provided by the Spanish Supercomputing Network (Red Española de Supercomputación), as well as the computer resources used: the LaPalma Supercomputer, located at the Instituto de Astrofísica de Canarias.

The author wishes to acknowledge the contribution of the IAC High-Performance Computing support team and hardware facilities to the results of this research.

Abstract

Prominences are highly dynamical solar structures that have yet to be fully characterized. In addition to the observations, theoretical studies and numerical simulations are essential to understand the physics governing their creation and evolution. In this work, we aim to shed light on how a coronal shock generated by a sudden energy release (like a flare) propagates along the magnetic field lines, impacts a prominence, and sets it into oscillatory motion. To that end, we have first studied the propagation of shocks and their interaction with a modeled prominence in a one-dimensional framework. We have obtained that the system tends toward a simple asymptotic configuration that can be physically understood. We extended the existing theory about shocks under thermal conduction effects, obtaining numerical solutions for their time evolution starting from a localized heat-deposition event, and, also, using simple initial profiles, their asymptotic trend toward those found in the earlier analytical studies. Finally, we performed two-dimensional simulations in which a prominence is self-consistently formed and a sudden energy release at a footpoint of the filament channel generates a perturbation of shock type. We studied the perturbation propagation and impact in detail for the first time. Applying the foregoing results to the solar case, we concluded that the impact of a coronal shock generated by a flare-like explosive event can produce large amplitude longitudinal prominence oscillations, with parameters in agreement with observed values.

Resumen

La atmósfera solar es un entorno altamente dinámico. El plasma que la compone exhibe propiedades variadas a diferentes alturas que permiten dividirla en fotosfera, cromosfera y corona, pero todo se encuentra en constante interacción debido al poderoso campo magnético.

Las prominencias (llamadas filamentos cuando se observan sobre el disco solar) son grandes estructuras de plasma frío y denso (de características cromosféricas) que se encuentran suspendidas en la corona sobre líneas de inversión de polarización. La estructura cizallada del campo magnético sobre estas permite la flotación del material denso y lo aísla del plasma coronal caliente. Las prominencias son altamente dinámicas y se han observado numerosos eventos oscilatorios [Arregui et al. 2018], excitados mediante llamaradas lejanas o mediante liberación de energía en regiones magnéticamente conectadas con la prominencia. Estos últimos eventos excitan oscilaciones longitudinales de gran amplitud (LALOs o simplemente LAOs), que serán el objeto del presente trabajo.

El estudio de las oscilaciones de prominencias es de gran interés, ya que se han clasificado como precursores de eyecciones de masa coronal, fenómenos de gran influencia en el clima espacial. Existen modelos teóricos variados según la generación de la prominencia, la configuración del campo magnético y el desencadenante de las oscilaciones. Sin embargo, no existe un estudio teórico en detalle sobre la propagación de energía a lo largo de las líneas de campo conectadas con las prominencias, y estas perturbaciones se postulan como agentes relevantes en la generación de oscilaciones.

Motivado por las observaciones e investigaciones actuales [Luna et al. 2024], en el trabajo expuesto a continuación estudiaremos la formación de una protuberancia, la generación de una perturbación energética, su propagación e impacto, y las consecuentes oscilaciones causadas. El estudio se elaborará mediante simulaciones numéricas de creciente complejidad realizadas con el código MPI-AMRVAC [Keppens et al. 2023], caracterizado por el refinamiento adaptativo y cálculo paralelo que favorecerá la conservación de los perfiles de choque. Para el procesado y análisis de los resultados de las simulaciones se creará un código Python versátil empleando el paquete `yt` [Turk et al. 2011].

En la Sección 2 se analiza la propagación e impacto de choques en el caso hidrodinámico unidimensional. El impacto es estudiado inicialmente desde una perspectiva analítica resolviendo el problema

de Riemann (2.1). El experimento *Sod shock-tube test* se desarrolla en 2.2 con el fin de validar el funcionamiento del código e introducir las herramientas para el estudio de resultados. A continuación, en 2.3 se analiza la propagación de choques y el impacto con regiones densas que simulan un filamento. Se detalla la propagación de perturbaciones secundarias que aceleran progresivamente al filamento, hasta que alcanza un estado asintótico en el que se propagará a la velocidad del medio post-choque inicial (2.4). Mediante un estudio paramétrico se valida la generalidad de las conclusiones. Por otro lado, en 2.5 se extiende la teoría de choques en presencia de conducción térmica [Zel'dovich and Raizer 1967; Lacey 1988] y se obtienen numéricamente los perfiles teóricos correspondientes. Mediante un experimento de calentamiento impulsivo se comprueba en 2.6 que la forma natural de los choques en presencia de conducción térmica corresponde con la predicha por la teoría, con perfil continuo en temperatura pero posible discontinuidad en densidad, presión y velocidad, además de un precursor térmico que se adelanta en la propagación.

En la Sección 3 se estudia el caso magnetohidrodinámico bidimensional mediante simulaciones en las que, debido a un mecanismo de evaporación-condensación, se genera un filamento suspendido en la depresión central de un campo magnético (3.1). A continuación se libera energía de forma impulsiva en uno de los pies de las líneas de campo que sujetan la prominencia, creando una perturbación tipo choque que se propagará a lo largo de las mismas líneas hasta alcanzar la prominencia. En 3.2 se estudia la propagación del choque, y se establece que, en caso de ser más homogéneo el camino, se propagaría con el perfil teórico esperado de choques bajo efecto de conducción térmica. El estudio abarca también el impacto de la perturbación con el filamento y las consecuentes oscilaciones que este último describirá en 3.3. Se identifica el periodo, la amplitud y el amortiguamiento a lo largo de líneas de campo a diferentes alturas, y se compara con los valores esperados de periodo según el modelo del péndulo [Luna and Karpen 2012]. En 3.4 se obtienen resultados compatibles tanto con el modelo del péndulo como con observaciones realizadas.

Finalmente, en el presente trabajo se concluye que los choques coronales generados por eventos explosivos tipo llamarada pueden desencadenar oscilaciones de prominencias. El modelo propuesto reproduce los resultados observacionales reportados por Luna et al. 2024. Creemos que muchas observaciones en las que no se identifica el detonante de una oscilación se podrían explicar mediante el presente modelo.

Contents

Abstract

1	Introduction	1
1.1	Objectives	3
1.2	Methodology	4
2	One-dimensional simulations	5
2.1	Analytical solutions: jump relations and the Riemann problem	5
2.2	Sod shock-tube test	6
2.3	Basic prominence simulations	9
2.4	Integrated quantities. Asymptotic state	14
2.5	Introduction of thermal conduction	18
2.6	Impulsive heating perturbation	19
3	Two-dimensional simulations	22
3.1	Prominence formation	22
3.1.1	Initial conditions	22
3.1.2	Simulation evolution	23
3.2	Impulsive heating, propagation and impact	25
3.2.1	Impulsive heating set-up	25
3.2.2	Perturbation propagation	25
3.3	Prominence oscillations	29
3.4	Comparison of 2D simulations and observations	32
4	Conclusions	34
A	Unit handling with AMRVAC	35
B	Effect of the thermal conductivity on the shock profiles	36
B.1	Solution of the ODE	37
B.1.1	Dimensionless solution	37
B.1.2	Dimensionalization of the solution	38
B.1.3	Jump relations	40
C	Thermal conduction in 2D coronal shocks	41

1 Introduction

The solar atmosphere is a highly dynamical environment. It is composed by plasma, which exhibits different behavior throughout its height, allowing to distinguish between photosphere, chromosphere and corona. Each layer is characterized by the state of the plasma and its consequent interactions with the Sun's magnetic field, leading to a diverse range of dynamical phenomena that exert influence on the surrounding medium.

Prominences (also known as filaments, when observed on the disk, so both names will be used interchangeably along the text) are large structures suspended in the solar corona, much cooler and denser than the ambient plasma. They are found above polarity inversion lines (PILs), which are the boundary lines separating opposite polarities of the photospheric magnetic field. A sheared magnetic field extends above this region, known as a filament channel, and is covered above by magnetic loop arcades with roots on both sides of the channel. This complex magnetic structure provides support against gravity for the cold and dense plasma of the filament and isolates it from the hot surrounding corona.

Solar prominences are highly dynamic structures, and there has been a number of observations reporting the presence of oscillatory motion [see review by Arregui et al. 2018]. These oscillations can be divided into two main groups. The first group consists of small-amplitude oscillations, generally with velocities below 10 km/s. These are local oscillations where different regions oscillate with different phases. They are thought to be excited by photospheric or chromospheric motions. The other main group is known as large-amplitude oscillations. These are typically global oscillations of the filament, where most of the structure participates in the oscillation. They are produced by energetic events such as flares or jets. They typically have velocities above 10 km/s and are referred to as **large-amplitude oscillations (LAOs)**. However, oscillations produced by flares can sometimes exhibit velocities below this threshold (see e.g. Luna et al. 2018).

LAOs can consist of periodic motions either perpendicular to or along the magnetic field. The first are transverse modes, and the second are longitudinal modes. A third possibility is mixed-polarity modes. The subject of this study is large-amplitude longitudinal oscillations (LALOs). Two groups of energetic agents that trigger LAOs can be distinguished. A first group of perturbations is associated with distant flares, triggering transverse, longitudinal, and mixed-polarity oscillations. A second group of agents is associated with subflares, microflares, or jets, magnetically connected to the filament, so that they only trigger longitudinal perturbations. This work is motivated by a recent observation by Luna et al. 2024. The authors report that a flare produces a large LALO with velocities above 70 km/s. The authors suggest that very hot, high-pressure plasma from the flare is injected into the filament channel, triggering the oscillation of the prominence. How this perturbation propagates through the filament channel and interacts with the prominence remains unknown. In this work, we aim to shed light on this process.

Prominences are relevant because they are the birthplace of most coronal mass ejections (CMEs), resulting in hazardous space weather conditions that can threaten human society. Observations have allowed the characterization of these structures, but there are many unsettled issues about their support and stability, the mass flows, radiative losses, the magnetic field, their formation and their disappearance [Parenti 2014]. The limited information obtained from observations has to be compensated by a specially dedicated effort on the side of the theoretical modeling. Analysis of oscillatory motion and contrast with theoretical models, the so-called prominence seismology, can provide useful information about the configuration of the magnetic field and other magnitudes that we are not able to infer directly from observations.

The use of advanced numerical methods is necessary to establish and test theories that enable us

to explain the behavior of these magnetized fluids due to the highly non-linear nature of their governing equations. There are many different codes in the state-of-the-art of numerical modeling for solar physics, like Mancha3D [Felipe et al. 2010], MuraM [Vögler et al. 2005, Rempel 2017], Bifrost[Gudiksen et al. 2011] or MPI-AMRVAC [Keppens et al. 2023]. They all solve the non-ideal magnetohydrodynamic (MHD) equations, with differences in the approaches or methods used to solve them.

Over the past few decades, the number of LAO observations has increased thanks to the capabilities of new telescopes. Transverse LAOs are associated with the restoring force of the magnetic field, the Lorentz force. Hyder 1966 and Kleczek and Kuperus 1969 developed the first models for horizontal and vertical oscillations, respectively. However, in longitudinal oscillations (LALOs), the Lorentz force does not play a role. Luna and Karpen 2012, Zhang et al. 2012, and Luna et al. 2012a proposed that the restoring forces in LALOs are a combination of gravity projected along the magnetic field lines and gas pressure gradients. Furthermore, they found that the gas pressure term is negligible under typical prominence conditions. These authors performed 1D simulations and analytical calculations and proposed the so-called pendulum model. Many additional one-dimensional studies of oscillations in prominences have been carried out, such as Zhang et al. 2013, Chen et al. 2017, and Ni et al. 2022, among many more. Numerical simulations in two dimensions have also been performed, as in Terradas et al. 2013, Luna et al. 2016, Zhang et al. 2019, Jerčić et al. 2022, or Liakh et al. 2023 as well as in three dimensions, as in Zhou et al. 2018.

However, only a few studies have considered the perturbation causing these oscillations. Some works introduce artificial perturbations, such as velocity impulses or impulsive asymmetric heating, as in Zhang et al. 2013 and Jerčić et al. 2022, or artificial pressure enhancements, as in Liakh et al. 2020; Liakh et al. 2021. In these cases, the perturbations eventually trigger the oscillations in the prominences. In another group of studies, the perturbations are generated in a self-consistent manner. For example, Luna and Moreno-Insertis 2021 produced a jet inside a filament channel that impacted the filament, exciting the oscillations. More recently, Liakh et al. 2023 simulated the eruption of a magnetic flux rope that generated an EIT wave, which reached a prominence and excited its oscillations. However, only a few studies have addressed how perturbations propagate within the magnetic structure of the prominence, the filament channel. Moreover, none of these studies have considered this propagation under non-adiabatic conditions.

Motivated by the recent observations reported in Luna et al. 2024, which indicate that hot, high-pressure plasma produced by a flare can travel along a filament channel and trigger LALOs, we have carried out a series of numerical simulations to study this process. Although several works have analyzed the triggering of prominence oscillations using simplified or artificial perturbations, to our knowledge the propagation of more realistic shock-like disturbances along filament channels has not been explored yet. In this TFM, we aim to study how these perturbations propagate and interact with the prominence plasma, considering an energy release event that is magnetically connected to the filament. For this purpose, we use a self-consistent filament model formed through the evaporation-condensation mechanism. The simulations include pure shock type perturbations and localized thermal energy injections, and we analyze how they travel along the magnetic field lines and affect the filament structure. We study this first in a one-dimensional framework that allows detailed study of fundamental hydrodynamic features of the propagation of the strong perturbations and their interaction with the filament, and then in two dimensions, which allow a more realistic scenario to study the filament and its surroundings. In Section 2 we study the 1D problem. We carry out hydrodynamic simulations of the impact of a coronal shock perturbation on a dense region resembling a prominence. Additionally, we simulate an energy release event and study the generated perturbations and their theoretical profile under thermal conduction effects. In Section 3 we carry out a 2D magnetohydrodynamic simulation in which, first of all, a prominence is

generated by the classical evaporation-condensation mechanism. Then, energy is released impulsively in a region magnetically connected to the prominence. We then study the propagation of the perturbation along the field lines, the impact on the prominence and the subsequent oscillations. All these numerical simulations will be performed using the MPI-AMRVAC code; a `python` tool will also be created from scratch in order to represent and analyze the data obtained from the simulations.

1.1 Objectives

The objectives of the present work are as follows:

- Development of a simple theoretical framework to analyze the interaction between large coronal perturbations (as resulting, e.g., from flares) and prominences. This modeling process is divided into two phases: (1) a 1D hydrodynamic study and (2) a more complete 2D model with self-consistent prominence formation.
- First part: development and analysis of 1D, hydrodynamic numerical simulations of shock waves impacting high-density compact regions mimicking solar filaments. Understanding of the complex interaction of the perturbed coronal medium with the filament via shocks and rarefaction waves.
- Additional preparatory study: theoretical investigation of shock propagation under thermal conduction effects, which are of importance in the solar corona. Asymptotic trend toward the analytical solutions of Lacey 1988.
- Second part: 2D magnetohydrodynamic models for the interaction of large coronal perturbations and filaments. (a) Formation of a filament through evaporation flows. (b) Perturbations caused by a large, localized energy release. Propagation along the magnetic field lines connected to the filament and impact the latter. (c) Study of the filament oscillations; comparison with the results of the pendulum model.
- Comparison of theoretical and numerical results with observations. Assessment of the similarities and differences between the perturbations and oscillations obtained in this work and those in catalogue data and reported events.
- In terms of technical training: Introduction to the multidimensional numerical simulation of physical processes in the solar atmosphere. Familiarization with a state-of-the-art numerical code, the MPI-AMRVAC code, through 1D and 2D (magneto)hydrodynamic test experiments. Construction of basic representation and analysis tools.

1.2 Methodology

The subject of this Master’s Thesis is of theoretical/numerical nature. Thus, the methods used are those associated with designing and executing numerical experiments, with a-posteriori analysis trying to understand the physical essence of the results and then checking whether those can be applied to understanding the solar phenomena targeted in the study. Therefore, concerning methods, two primary ones to mention in this section are those related with the numerical code used to carry out the experiments and those used for the a-posteriori analysis.

This Master’s Thesis uses a state-of-the-art numerical code, the MPI-AMRVAC code, that is being employed by different researchers in the world to perform hydrodynamic and magnetohydrodynamic simulations of, sometimes, great complexity. MPI-AMRVAC is a parallel, adaptive mesh refinement framework primarily aimed at solving hyperbolic-parabolic partial differential equations, with emphasis on guaranteeing the fulfillment of the conservation laws and capturing shock fronts. These two features make it a code of choice for solving the problem posed in this work.

MPI-AMRVAC was created as a versatile code with options and switches for its application to various problems, allowing the user to easily change multiple parameters of the simulations, ranging from the numerical scheme to the various possible ingredients to be used in the calculations. This characteristic will permit us to easily increase the complexity of the developed simulations, activating magnetohydrodynamics, thermal conduction or radiative cooling as needed. The code is written in Fortran 90 and uses MPI for parallelization. A basic knowledge of Fortran is required on the side of the user to be able to write simulation set-ups and run them. Additionally, the source code must sometimes be studied in order to understand its behavior. Concerning MPI, the most complex simulations that have been carried out in this Master’s Thesis would require hundreds of hours of computational time if executed in a single CPU. Therefore, the parallelization scalability of MPI-AMRVAC is exploited by making use of the IAC High-Performance Computing facilities and the LaPalma Supercomputer.

The adaptive mesh refinement (AMR) algorithms of the MPI-AMRVAC code use a standard block-based octree scheme that splits cells wherever a refinement criteria is met. In the simulations developed we varied from 3 to 5 refinement levels depending on the needs, allowing us to cover a large spatial domain without sacrificing the spatial resolution in regions with sharp transitions or gradients nor wasting computational time if a high-resolution regular grid had been used.

The results of the simulations carried out in this work were read with the Python library *yt* [Turk et al. 2011], which supports structured, variable-resolution meshes. Due to the specific analysis that we wanted to perform, the processing of the data was carried out with a Python class created in the framework of this work. This class allows us to read the snapshots generated by the MPI-AMRVAC simulations with the help of *yt* and then transform, calculate, represent and animate the desired outcome. A great effort has been put into the creation of this Python tool keeping its versatility in mind, trying to create an easy-to-use utensil that will smooth the analysis process of future simulations. It deals with different tasks, such as writing to regular grids in order to compare space-time values, saving relevant time-consuming calculations to increase efficiency, determination of one-dimensional profiles along magnetic field lines in two-dimensional simulations or creation of different types of data visualization.

2 One-dimensional simulations

The first set of simulations performed with the MPI-AMRVAC code is one-dimensional. All variables depend on a single coordinate, x , and motion is restricted to that direction. The numerical method employed is the *Total Variation Diminishing Lax-Friedrich* (TVDLF) scheme. It is a robust method, with no spurious oscillations when dealing with discontinuities, but it can be more diffusive than other available methods. The boundaries of the spatial domain were chosen open for all conservative variables, meaning that the gradient is kept zero at the edges by copying the edge value into the ghost cell. The implications of this boundary condition will be seen below. Regarding the mesh, three refinement levels were used: this implies that, when gradient values are too large, the code can split certain cells in half up to two times. The number of grid points used for the base level in these simulations was 2048.

The initial 1D simulations were performed with dimensionless values. Appendix A explains how AMRVAC treats units and how the output data in code units can be converted to physical units in the CGS system. Thermal conduction and radiative cooling will be activated in the final simulations in this section: 2.5, 2.6 as well as in the 2D simulations, Section 3.

In this thesis we aim to study the impact of a coronal jet onto a prominence. This will be modeled through a shock perturbation propagating in a coronal medium that impacts onto a compact region of chromospheric density and temperature. As initial condition for the 1D problem, therefore, we will use an incoming shock with temperature jump of 10, impacting onto a prominence which is 100 times denser than the pre-shock medium and in pressure and velocity equilibrium with it. These ratios are representative of values actually encountered in observed episodes of flare perturbations impacting on a filament in the Sun (see Benz 2008; Luna et al. 2024).

A note of interest concerns the applicability of the experiments in this chapter to cases with non-zero magnetic field: given the one-dimensional nature of the experiments, the longitudinal component of the magnetic field must be constant (to preserve the condition of solenoidality of the field). On the other hand, in this thesis we are interested in the impact on filaments of large perturbations that propagate along the field lines. Therefore, in the 1D study of this chapter we will not be covering the case in which the magnetic field has a transverse component. In 1D cases with a longitudinal field exclusively there is no Lorentz force and the magnetic field does not play any role in the dynamics or energetics of the system. So, the simulations here, although purely hydrodynamic, can be applied to simple magnetized situations in the corona. In fact, this applies also to a limited extent to the 2D case if the magnetic field is strong enough, i.e., if the motion is fully channeled along the field lines.

2.1 Analytical solutions: jump relations and the Riemann problem

Shock waves are sharp transitions in the physical quantities of a fluid propagating with speed higher than the sound speed of the pre-shock medium, and are a consequence of the non-linear terms of the fluid equations. The equations that describe hydrodynamic shock waves and provide the jump relations across them can be found in many basic books on hydrodynamics or magnetohydrodynamics, like Priest 2014 or Zel'dovich and Raizer 1967. Studying the system in a frame of reference at rest with the shock wave, labeling the density, pressure and velocity of the unshocked gas as ρ_0 , p_0 , u_0 , and those of the shocked gas as ρ_1 , p_1 , u_1 , then the sonic Mach number is defined as $M_0 = |u_0|/c_{s0}$, where $c_{s0} = \sqrt{\gamma p_0/\rho_0}$ is the sound speed of the pre-shock medium. For the simplest ideal gas, the jump relations across a shock in

terms of the pre-shock state and the Mach number are given by:

$$\frac{p_1}{p_0} = \frac{2\gamma}{\gamma+1} M_0^2 - \frac{\gamma-1}{\gamma+1}, \quad (2.1)$$

$$\frac{\rho_0}{\rho_1} = \frac{2}{\gamma+1} \frac{1}{M_0^2} + \frac{\gamma-1}{\gamma+1}, \quad (2.2)$$

$$M_1^2 = \frac{2 + (\gamma-1)M_0^2}{2\gamma M_0^2 - (\gamma-1)}, \quad (2.3)$$

with γ the adiabatic index. These relations will be used to test the proper functioning of the code employed in this thesis.

To understand the impact of shocks onto dense region recourse must be had to the well-known classical Riemann problem, which is a set of fundamental solutions of the nonlinear system of equations of hydrodynamics in one spatial dimension. It is defined as an initial value problem in which the initial conditions consist of two uniform domains in density, velocity and pressure separated by a discontinuity. In the general case, the result will be a nonlinear wave of shock or rarefaction type propagating to the left, another one propagating to the right and a contact discontinuity between them, i.e., a jump exclusively in the density and temperature that is co-moving with the fluid and separates the left and right regions. A good exposition of the theory of the Riemann problem in 1D hydrodynamic situations characterizing the left and right perturbations and the jumps of the fluid can be found in Toro 2009.

The analytical solution of the Riemann problem will be used as a solid basis to test the accuracy of the numerical solution obtained with the AMRVAC code; to that end we shall first solve a simple type of Riemann problem, namely, the Sod shock-tube test (Section 2.2). Then, in Section 2.3, we shall use the solution of the Riemann problem for the physical interpretation of the result of the impact of the shock on the prominence.

2.2 Sod shock-tube test

The MPI-AMRVAC code will initially be tested with a relatively simple form of the Riemann problem, namely the Sod shock-tube test, shown in Figure 1. Its initial condition consists in a one dimensional fluid at rest with different (uniform) values of pressure and density on either side of a membrane and zero velocity throughout, as indicated by the black dashed line in the figure. When the membrane is removed, a **shock** propagates into the domain with lower density, a **rarefaction wave** moves in the opposite direction, and a **contact discontinuity** remains, co-moving with the fluid in-between the two other nonlinear waves.

The initial condition is defined by $\rho_A = 3$, $p_A = 4$ and $v_A = 0$ to the left of the membrane and $\rho_E = 1$, $p_E = 1$ and $v_E = 0$ to the right, where the sub-index is chosen according to the different regions labeled in the following figures. A video animation of the solution we obtain for that initial condition can be seen here: [Video 1¹](#). A set of vertical dotted lines represent the Lagrangian tracing of four test-particles in the video. According to the analytical expressions described in Toro 2009 (page 119), the expected results are as follows: a **rarefaction wave** will propagate to the left with local sound speed $c_{sA} = 1.49$ separating regions **A** and **C**. A **contact discontinuity** will separate regions **C** and **D** and a **shock** will propagate to the right with supersonic speed $V_{sh} = 1.78$, equivalent to a sonic Mach value of $M_0 = 1.34$. The predicted state for the different regions is shown in Table 1. It is trivially checked that the numerical values and propagation velocities match the expected values, and the rest of this section will be dedicated to understanding the time evolution of the different resulting perturbations.

In order to analyze and comprehend the experiment just mentioned, (and, in fact, for other experiments in this thesis), we have developed various numerical and graphical tools. Specifically, they

¹https://drive.google.com/file/d/1tFhj4bCFQSqt_PIIaKj6ZMhM_-QwMtca/view?usp=share_link

	A	C	D	E
ρ	3.00	1.98	1.50	1.00
p	4.00	1.99	1.99	1.00
v	0.00	0.58	0.58	0.00
c_s	1.49	1.29	1.49	1.29

Table 1: Analytical solution of the Riemann problem for the resulting regions of the simulated Sod shock-tube experiment.

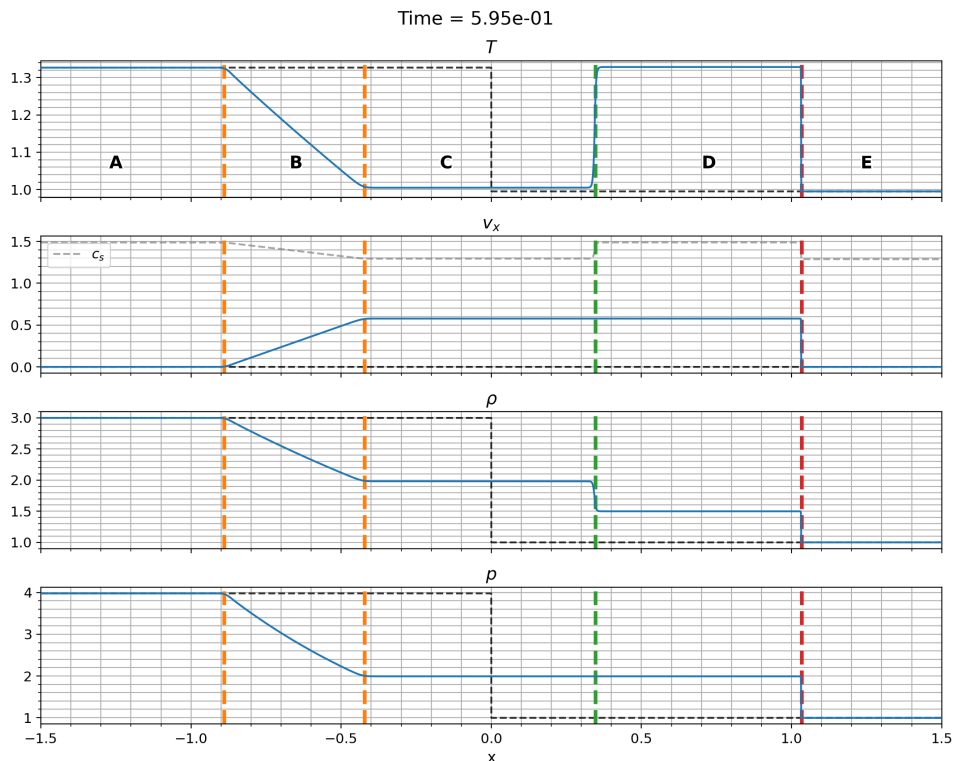


Figure 1: Sod shock-tube test. The four panels represent the values of temperature, velocity along the x axis, density and pressure. The black dashed line represents the initial conditions, while the blue line represents an evolved snapshot. The gray dashed line in the velocity plot represents the local sound speed. The vertical colored dashed lines indicate the position of the different perturbations, namely, the **rarefaction head and tail**, the **contact discontinuity** and the **shock**. The black letters mark the areas delimited by the different perturbations, as indicated in the text.

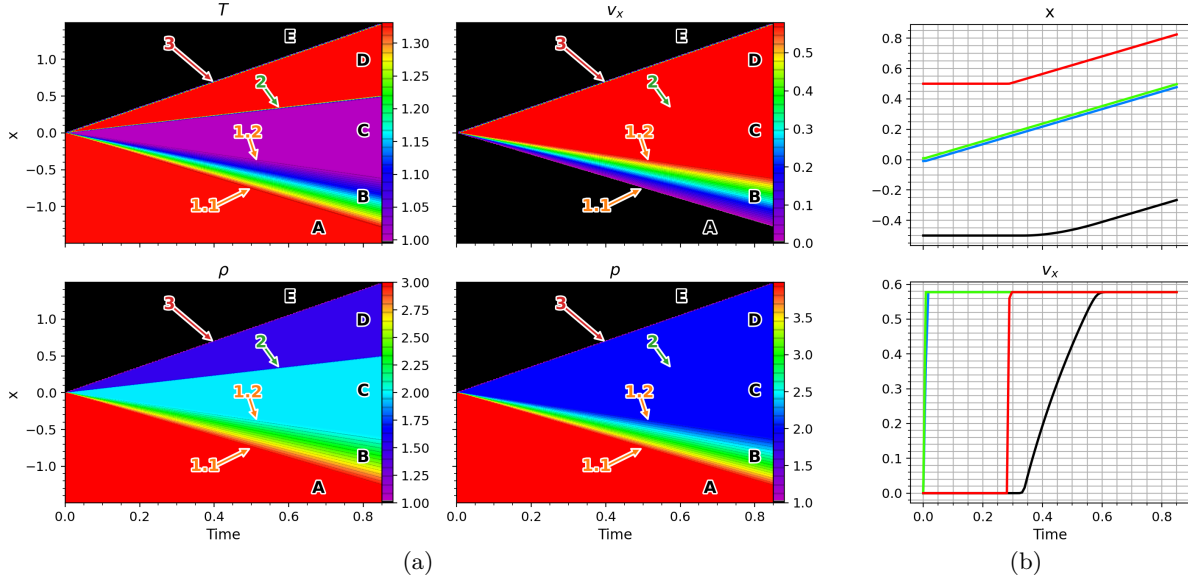


Figure 2: Analysis of the Sod shock-tube test simulation. 2a shows the space-time plot of temperature, velocity, density and pressure. The characteristic perturbations are labeled with numbers 1 to 3, indicating the **rarefaction head** and **tail**, the **contact discontinuity** and the **shock**. The black letters mark the areas delimited by the different perturbations. 2b represents the Lagrangian tracing of position and velocity of test particles visible in the video animation.

are the representation of a particular snapshot (Figure 1), the space-time diagrams of the simulation (Figure 2a) and the Lagrangian tracing of different magnitudes (Figure 2b).

The three figures should be analyzed together to interpret the experimental results. Regarding Figure 1, the blue lines describe the state of an advanced snapshot of the Sod shock-tube test simulation, while the black dashed lines depict the initial conditions. The gray dashed line in the velocity plot represents the local sound speed. The vertical dashed lines indicate the position of the different perturbations described in the previous paragraphs and which will be identified by color in the following. The regions delimited by the perturbations are labeled as **A**, **B**, **C**, **D** and **E**.

Regarding Figure 2a, a space-time plot is shown for the different variables. The vertical axis corresponds to the spatial dimension while the horizontal axis corresponds to the time. The color indicates the value of each variable according to the color-bar next to each plot. A set of colored number tags identify the different perturbations, while the black letters indicate the regions delimited by them, in agreement with Figure 1. The description of the different perturbations is as follows:

1. The **rarefaction wave** propagating to the left. This is a decompressional wave that propagates at the local sound speed.
 - 1.1 The head of the rarefaction wave travels through the high-density and high-pressure medium (labeled **A**) with the local sound speed. It increases the fluid velocity in the opposite direction (to the right), while decreasing density and pressure.
 - 1.2 The tail of the rarefaction wave finds the medium where pressure and density have already decreased. The local sound speed is lower there (see dashed gray line in velocity plot of 1) so its propagation speed is lower than that of the tail. Figure 2a clearly illustrates how the head and tail separate through time. They delimit the region **B** where progressive decompression and fluid acceleration resembles a color fan visible in all subplots.

Behind the rarefaction tail a region of constant value is labeled as **C**.

2. The **contact discontinuity** propagates to the right co-moving with the fluid, separating regions **C** and **D**. It can be seen from both Figures 1 and 2a that it only involves a jump in density but constant pressure and velocity, which is a major feature of the contact discontinuities. Temperature will therefore jump too.
3. The **shock** propagates to the right with supersonic constant velocity, causing a sudden increase for all variables (sharp jump visible in every panel of Figures 1 and 2a) separating the pre-shocked and post-shocked regions (**E** and **D** respectively).

Figure 2b displays the results of the Lagrangian tracing for the position (top panel) and velocity (bottom panel) of four test particles initially placed at -0.5 , -0.009 , 0.009 and 0.5 . Their motion can be followed by the dotted lines of the video animation [Video 1](#)). The first two of them (black and blue lines) are placed in the high-density medium, one of them far away from the membrane and the other very close to it (36 grid-points away), while the last two (green and red) are placed in the low-density medium at an equivalent distance from the membrane. Analyzing the Lagrange tracers from left to right, it can be seen from both panels of Figure 2b that:

- The black tracer remains static until it is reached by the rarefaction head at $t = 0.34$ (i.e., in region **A**). At that point, the fluid element begins moving to the right but, exactly following the physical nature of a rarefaction wave, not via a sudden jump but, rather, gradually, as the wave moves over it, with decreasing density and increasing velocity as time advances (i.e., flowing through region **B**) until the wave leaves behind the tracer and it remains in region **C**.
- The blue tracer is placed closely to the left of the membrane (region **A**). When the membrane is removed, the rarefaction wave rapidly reaches it when it has not expanded much, causing a quick but not sudden velocity increase. Then, the tracer remains in region **C** very close to the left of the contact discontinuity.
- The green tracer is initially in region **E**. As soon as the experiment begins, the shock reaches it and causes a sudden increase of velocity, density and pressure, transitioning to region **D** and moving very close to the right of the contact discontinuity.
- The red tracer, initially far away from the membrane, remains static in region **E** until the shock impacts it at $t = 0.28$, experiencing a jump in density and velocity and transitioning to region **D**.

2.3 Basic prominence simulations

To understand the basic physical properties of the interaction between an incoming coronal shock and a dense chromospheric filament we carry out in this section 1D hydrodynamic simulations that contain basic elements of that astrophysical problem: we launch a shock propagating in a medium with coronal temperature that advances towards a region with very dense and cool plasma mimicking the filament, as can be seen in the videos: [Video 2a](#)² and [Video 2b](#)³. Following the methodology of Section 2.2, we will work with dimensionless values. In order for the solar scalings between chromospheric and coronal temperatures and densities are preserved, the chosen values fulfill the following conditions: we choose for the modeled prominence values of density and temperature which are 100 times higher (the density) and lower (the temperature) than the ambient coronal medium; on the other hand, again to preserve the order of magnitude of the values encountered in the solar problem, the incoming shock will have a temperature jump of one order of magnitude. To that end, a Mach number of the initial shock of 5.41 is required,

²https://drive.google.com/file/d/1fxHRMoRrh-qkFQkbOSUAMGHkXydvphLY/view?usp=drive_link
³https://drive.google.com/file/d/1iDRAtZ4g1N04Cr6HRvIbyKd5q6an8_dh/view?usp=share_link

which is a value in the range observed in solar flares. The numerical results are shown in code units. To compare with solar values, one can choose the following set of three base units, namely $L_C = 10^9$ cm for length, $n_C = 10^9$ cm $^{-3}$ for particle number density and $T_C = 10^6$ K for temperature. As explained in Appendix A, all physical variables are divided by those units or by the derived units obtained through combinations of them, like $V_C = 1.16 \cdot 10^7$ cm s $^{-1}$ = $1.16 \cdot 10^5$ km s $^{-1}$ for velocity, $\rho_C = 2.34 \cdot 10^{-15}$ g cm $^{-3}$ for density, $\tau_C = 85.9$ s for time or $p_C = 0.318$ dyn cm $^{-2}$ for pressure; the inverse process is done to convert results expressed in code units to physical (CGS) values.

The set-up of the first simulation consists of a spatial domain from $x = -750$ to $x = 800$ with open boundaries (ghost cells with zero gradient). The initial shock is placed at $x = -700$ and the modeled prominence is located between $x = 2$ and $x = 32$. The final time of the simulation is $t = 300$, which is just before any of the propagating perturbations reaches the boundaries of the domain. The basic grid has 4096 points and four refinement levels are used, implying a maximum spatial resolution of $\Delta x_1 = 0.126$. Later in the Section, a second simulation with increased domain and duration will be presented. This second simulation covers a spatial domain from -1500 to 9000 and is calculated until time $t = 1500$. The basic grid has 8192 points and five refinement levels are used; still, given the enlarged domain, this second simulation has worse spatial resolution ($\Delta x_2 = 0.160$) than the first one. The implications of the different numerical resolutions will be discussed in Section 2.4.

Concerning the initial conditions for the physical variables, the state of the unshocked medium (subindex 0) is specified as follows: $\rho_0 = 1$, $p_0 = 1$ and $v_0 = 0$, and thus $T_0 = 1$. The filament (subindex 'f') is given a density of $\rho_f = 100$, but it is set in pressure equilibrium with its surroundings, so its temperature is $T_f = 10^{-2}$. Also, like its surroundings, its initial velocity is zero. The density, pressure and velocity of the shocked medium (subindex '1'), i.e., to the left of $x = -700$, are set to $\rho_1 = 3.61$, $p_1 = 36.1$ and $v_1 = 5.05$; its temperature is thus $T_1 = 10$. This shock has incoming Mach number $M_0 = 5.41$, so it will propagate with speed $V_{sh0} = 7$ and reach the filament at $t \approx 100.3$.

In the present section the initial impact of the shock onto the filament and the propagation of the subsequent perturbations will be analyzed in detail using the first of the two simulations. To that end, in Figure 3a we present temperature, velocity, density and pressure profiles at various times; in Figure 3b the corresponding space-time plots for those variables are shown. The time evolution can be best seen in the accompanying animation [Video 2a](#) and it is important that the readers check the movie additionally to the figures. For the sake of clarity, in the figures a restricted spatial domain and a limited time interval are shown (e.g., from $x = -100$ to $x = 500$ and from $t = 90$ to $t = 250$ in Figure 3b). A set of six important events has been chosen to explain the main physical processes in the experiment starting (label '0') with the earliest time in the figure, namely $t = 90$.

0. The profiles at time $t = 90$ are drawn with blue lines in Figure 3a. The incoming shock is located at $x = -70$ at that time. The dense and cool region corresponding to the filament can be seen in the range (2, 32) in the space-time plot (Figure 3b) as a black band in the temperature panel (top left), and as a green band in the density panel (bottom left); at that time, the filament is still at rest and in pressure equilibrium with its surrounding medium, so no difference in color can be observed in the corresponding panels on the right in that spatial range at that time. The incoming shock can be seen at that time as the sudden jump in all variables at $x = -70$ and moving forward in the following instants.
1. At $t = 100.3$ the shock impacts the prominence, as indicated with the arrow labeled '1' in Figure 3b. The profiles for this time in Figure 3a, drawn in orange, (or, better, in the accompanying animation), allow us to conclude that the situation at the left boundary of the filament at this time can be considered a Riemann problem: two homogeneous regions are separated by a discontinuity, like the

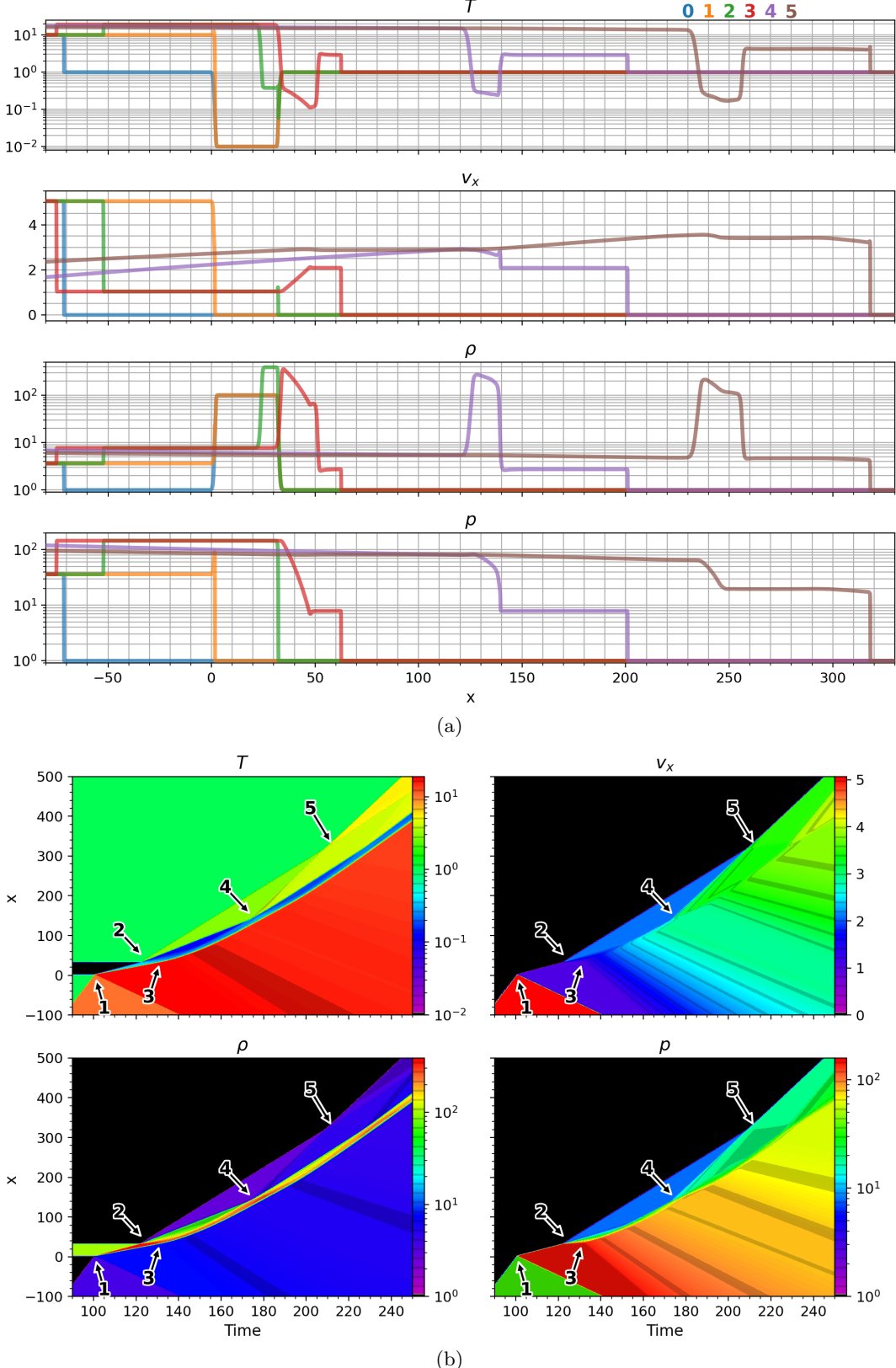


Figure 3: Basic prominence simulation. Figure 3a shows the profiles of the different variables at different instants of time. A video animation is available: [Video 2a](#). Figure 3b shows the space-time plot of the simulation, with the main events described in the text labeled from 0 to 5. Instant 0 corresponds to $t = 90$, the first time studied in this figure in which the initial shock is still propagating towards the static filament.

case studied in Section 2.2, except that now the domain to the left of the discontinuity has non-zero velocity, this is a more general Riemann problem than the simple Sod shock-tube experiment of that section. Applying the expressions given on page 119 of Toro 2009, the Riemann problem can be solved and the analytical values for the perturbations obtained. The result is that this situation evolves into (a) a shock propagating to the left with $M_{1,\text{left}} = 1.85$ and $V_{sh1,\text{left}} = -2.5$, i.e., a reflected shock, and (b) a shock propagating to the right with $M_{1,\text{right}} = 10.8$ and $V_{sh1,\text{right}} = 1.4$, which is a transmitted shock, leaving in-between a contact discontinuity co-moving with the fluid with $v = 1.04$. These three features can be located most easily by checking with the movie: viewing it from $t = 100.3$ onwards, one clearly sees the reflected shock moving to the left into the previously shocked gas, the transmitted shock advancing in the interior of the filament, and the contact discontinuity at the left boundary of the dense domain in a region with no discontinuity in pressure or velocity. It is interesting to see in the movie how the progression of the transmitted shock inside the prominence causes a density increase in it by a factor nearly 4, as expected for a strong hydrodynamic shock. The prominence is therefore gradually squeezed, and its total length decreases by that same factor by the time when the shock has gone across its full width.

Going now to the space-time plot (Figure 3b), the reflected shock can be seen particularly well in the velocity and pressure panels (top and bottom right panels) as the negatively inclined boundary of the red and green triangular domains which peak at the arrow labeled '1'. It is a little more difficult to locate the transmitted shock in that figure, but one can spot it in the density panel (bottom left) as the top boundary of the reddish wedge issuing from the arrow, with the contact discontinuity being the bottom boundary of that wedge.

2. At time $t = 121.7$ the shock propagating to the right through the prominence reaches its right edge. In the green profiles of Figure 3a the squeezed prominence can be seen, while the initial reflected shock is propagating away to the left. Here again, a new Riemann problem can be solved with the values right and left of the discontinuity. The resulting perturbation propagating to the left is now a rarefaction wave with velocity 0.25 for the head and 1.64 for the tail. Those two values are positive: even though the rarefaction wave moves to the left relative to the gas, the gas itself is moving to the right with speed 1.04, so it drags the whole rarefaction wave to the right as well. This is clearly apparent in the movie. The rarefaction wave keeps moving leftward relative to the prominence until it reaches its left boundary. A transmitted shock with Mach 2.56 and $V_{sh} = 3.28$ results which propagates to the right, and a contact discontinuity remains, co-moving with velocity 2.09. The rarefaction wave can scarcely be seen in the space-time plot as a tight color fan in all variables expanding from point 2 towards point 3. The transmitted shock can be seen as a sharp straight color boundary linking points 2 and 5. The right boundary of the prominence, which is a contact discontinuity, can be seen as a sharp transition in ρ and T only, propagating in a straight line from point 2 to point 4. After this event, the right edge of the filament travels faster than the left edge, decompressing it.
3. At time $t \approx 131$ the rarefaction head has reached the left edge of the filament. During its propagation, it has accelerated the prominence to the right. This impact cannot be modeled as a Riemann problem because it is not a sharp transition between two homogeneous media. Careful analysis of the movie Video 2a allows us to interpret the situation: the rarefaction wave is partly transmitted out of the filament and travels with sound speed to the left. Part of it is reflected to the right, and it can be seen that a shock forms. The filament compresses again while this new shock propagates across it. The left edge has increased its speed.
4. At time $t \approx 173$ the new shock has propagated across the filament and reached its right edge.

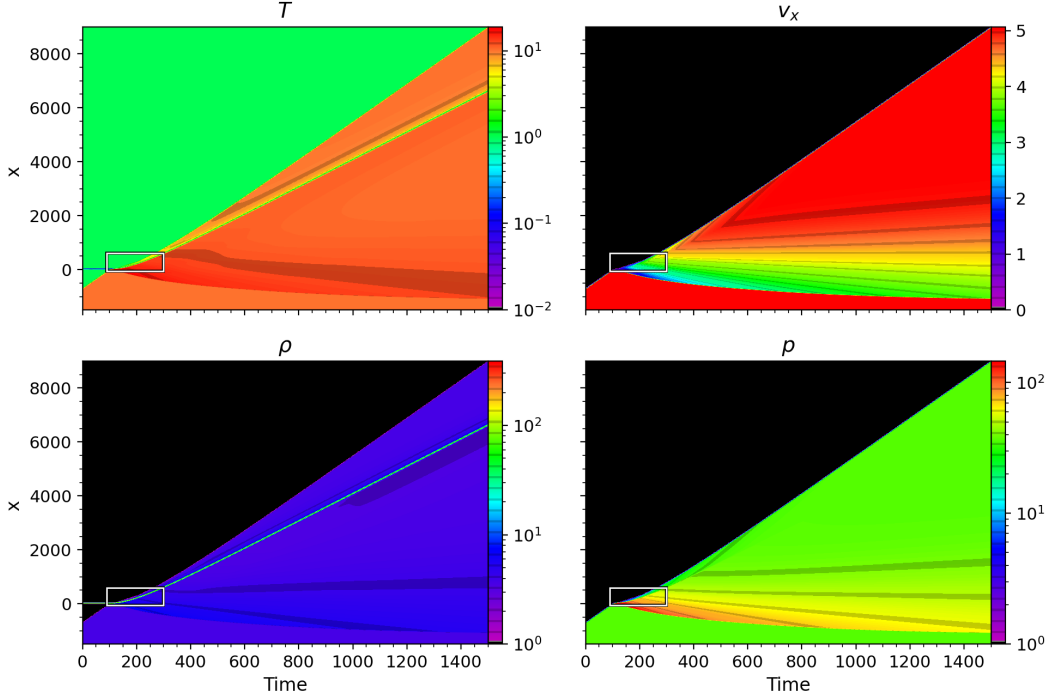


Figure 4: Space-time plot for the total simulation time. The domain included in Figure 3b is denoted by a white rectangle. The acceleration of the prominence can be tracked by change of slope of the bright curve in the density plot.

Like in event 2, a reflected rarefaction wave to the left and a transmitted shock to the right are created after the impact, leaving a contact discontinuity moving faster than before. The resulting perturbations can be seen in the space-time plot.

5. At time $t \approx 208$ the transmitted shock from event 4 reaches the transmitted shock from event 2, resulting in a stronger shock propagating to the right, a contact discontinuity and a rarefaction wave propagating left, which contribute to the acceleration of the filament.

Summarizing the information above, after the first impact (1) a shock is transmitted across the filament while another one is reflected to the left of it; the left edge of the filament begins moving to the right, compressing the prominence. When the transmitted shock reaches the right edge of the filament (2), a transmitted shock and a reflected rarefaction wave appear, while the right edge begins moving. The prominence decompresses as the rarefaction wave propagates across it leftward. When that wave reaches the left edge (3), it gets transmitted into the medium left of the prominence and a shock is created that moves to the right, compressing the prominence once again. This sequence of impacts and partial transmissions and reflections continues for some time: secondary perturbations propagate across the filament, compressing and decompressing it while always increasing its total velocity. The subsequent transmission of shocks to the right of the prominence increases the strength of the initially transmitted shock. As long as there is a pressure gradient across the filament (visible in Figure 3b, p plot), it keeps gaining speed. Nevertheless, the subsequent secondary perturbations have decreasing amplitude and after a finite amount of time the pressure gradient disappears and the prominence is not accelerated anymore.

To illustrate the above, Figure 4 is presented. It shows the space-time plots for the simulation covering a larger domain and with a much longer duration. The domain studied in Figure 3b is denoted by a white rectangle. The position of the filament can be tracked in the density and temperature plots as a distinctive thin line in green (temperature panel) or in blue (density panel). Right after the first

impact, the prominence begins moving with increasing speed (upwards curve in the space-time plots). After some time the curve straightens, i.e., the filament ends up moving with constant speed. Even if not easy to ascertain in the figure, the pressure gradient across the filament is small from about $t = 600$ onward, leading to the uniform motion of the filament.

In order to characterize the asymptotic state reached by the filament a study of integrated quantities in the filament and in the whole domain is performed in the following section.

2.4 Integrated quantities. Asymptotic state

For the purpose of concluding that the prominence in the simulation reaches an asymptotic state, further analysis is required. As a good indicator we choose to study the time evolution of integrated magnitudes in the filament and in the whole domain. To carry out the integration in the filament, the points in it were selected by filtering using a minimum-density threshold of $\rho = 10$, which is 10% of its initial density. Figure 5 shows the variation in time of the total integrated mass, momentum, width, internal, kinetic and total energy of the filament. Figure 5a shows the integrated variables for the time span analyzed in the previous section (Section 2.3), with colored vertical lines indicating the relevant events discussed in it. Figure 5b shows the integrated variables for the greater time-span simulation (second simulation, which had a much longer duration and was shown in the space-time plot of Figure 4 and animation [Video 2b](#)). The vertical gray lines in it denote the time-span covered in Figure 3b. As already remarked at the beginning of Section 2.3, the second simulation had a little worse numerical resolution ($\Delta x_1 = 0.126$ vs. $\Delta x_2 = 0.160$) than the first one. The implications will be discussed below.

Inspection of Figure 5a reveals the following: the mass of the filament is kept essentially constant (top-left panel) with maximum variation of 0.5% across the diagram (note the small range in the ordinates scale). The momentum (top-central panel) increases at a high rate after first impact (event 1) and more slowly as time advances. The width of the filament (top-right panel) is minimum when the first transmitted shock has propagated through it, as we can expect from the discussion in Section 2.3, and then oscillates as the succession of shocks and rarefaction waves sweep across it. The total internal energy of the filament (bottom-left panel) is basically the integral of the gas pressure across it. The changes are due, first, to the initial compression (maximum at event 2) and the subsequent oscillations are due to the secondary perturbations, with decreasing amplitude. The kinetic energy (bottom central panel) has a slow start, as the filament is progressively getting into motion, but the secondary perturbations contribute to its acceleration. Finally, the total energy (i.e., the sum of the kinetic and internal energies, see bottom-right panel) is dominated by the continuous growth of the kinetic energy, as the internal energy is small compared to it and stabilizes quickly around a final asymptotic value. In fact, the smallness of the internal versus the kinetic energy is simply tied to the fact that the filament is moving at supersonic speeds soon after the passage of the first shock wave (event 2).

In order to come to conclusions about the asymptotic state of the filament, Figure 5b, has to be analyzed. It shows the evolution of integrated variables in the filament for the second simulation. The mass is still close to constant in time (max variation of about 1% throughout the whole experiment) in spite of the worse resolution of this simulation ($\Delta x_1 = 0.126$ vs. $\Delta x_2 = 0.160$). The inspection of the momentum, and thus kinetic and total energy, reveals that the filament is accelerated until $t \approx 600$, when it reaches an asymptotic velocity. The width of the filament oscillates in the first phases of the time evolution, when the filament is being swept by the succession of shocks and rarefaction waves, until about $t = 400$. Thereafter, the width increases monotonically by a non-negligible amount, close to 20%. This is due to the fact that the sharp boundaries of the filament are being smoothed by numerical diffusion. While this does not have an impact on the total mass, momentum or kinetic energy, it clearly shows in the width profile Figure 5c shows the average values of temperature and velocity across the filament. Its

temperature has increased by a factor of 25, but is still quite below the coronal temperature (100 times hotter). The velocity grows until $t \approx 600$ and finally reaches an asymptotic value of $v = 5.05$. It is of interest to compare that value with the velocity we imposed on the post-shock medium in the initial condition ($t = 0$), namely $v_1 = 5.05$. In other words, the asymptotic velocity of the filament after being impacted by a shock and affected by all the subsequent shocks and rarefaction waves that go back and forth across it is that of the post-shock medium of the initial shock. This clearly indicates that a basic physical process is at work.

The explanation for the simple long-term dynamics of the simulation can be given as follows. The initial shock impacts the filament and sets it into motion, and a series of secondary perturbations will propagate back and forth across it. In the experiment we are assuming that the gas coming into the domain through the left boundary has constant speed, as if a piston were pushing the gas to the right. This mechanism is injecting momentum into the domain. As soon as the prominence is crossed by the original shock, it, in some sense, is part of the post-shock medium, but with a different velocity. So the subsequent series of shocks and rarefaction waves hit the filament and cause a global positive acceleration of its center of mass. This process gradually ends as the filament velocity increases and reaches the same speed as the original postshock medium. By then, the situation becomes extremely simple, as apparent in the right half of the panels in Figure 4: the filament just co-moves with the postshock medium of the initial shock, and the latter just advances with the same characteristics (e.g., $M_0 = 5.41$) that it had at the very beginning of the experiment At that point, the total momentum entering the domain through the left boundary will be invested in raising the momentum of the pre-shock medium, even though now this happens on the right side of the filament. The result can be seen in [Video 2b](#), where a set of horizontal red lines have been included, marking the initial post-shock state for all variables. It can be appreciated that the final shock propagates with exactly the same values of the incoming initial shock.

This interesting result motivates us to perform a parametric study. We have repeated the same experiment with different parameters for the initial shock, exploring Mach numbers from 1.5 to 9.6, which is equivalent to temperature jumps across the shock from 1.5 to 30. From those experiments we can conclude that the filament reaches constant velocity equal to that of the initial post-shock medium in all cases. Only a variation of the time required to reach the asymptotic state is found, with shorter times obtained for stronger initial shocks. This result is predictable, due to the faster propagation speeds of stronger perturbations across the filament.

In order to numerically prove the previous statement, Figure 6 is presented. It shows three plots that compare the velocity, density and pressure of the initial post-shock values (horizontal axis) versus their final values around the filament. A close inspection of the final state of [Video 2b](#) shows that there is a visible density difference to the left and to the right of the prominence, so both values are included in the Figure. Different colored crosses represent the different simulations performed, labeled by the sonic Mach number of the initial shock. It can be seen that the final values of velocity and pressure around the filament are identical to those originally in the post-shocked medium. In contrast, final density resembles that of the original post-shocked medium only to the right of the filament. It can be seen that the left-side values fall to an 86% of the original density. The density deficit is due to the reflected rarefaction wave that propagates towards the left of the filament.

These tests were repeated two times, reducing in half and doubling the initial thickness of the prominence and the results obtained were identical: a stationary state is reached after perturbations are reflected through the filament for a while, with final velocity and pressure identical to the initial post-shock values and a step in the density to the left of the filament. The only difference observed was in the time required to reach the asymptotic state, higher for thick prominences and lower for thin ones, due to the extra time required for perturbations to travel from one extreme of the prominence to the other.

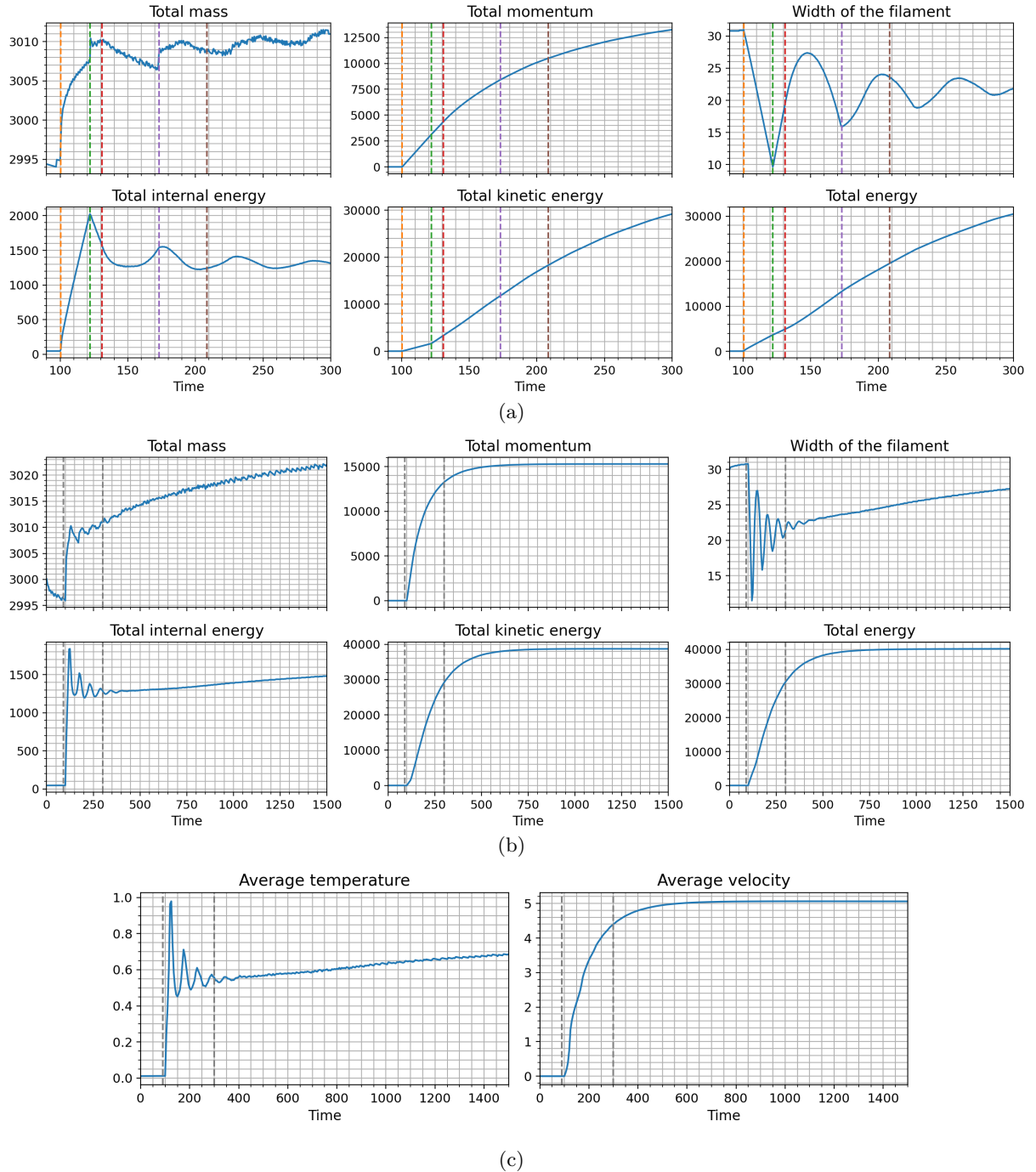


Figure 5: Figure 5a shows the integrated variables across the filament for the first simulation. The colored vertical lines represent the times of the relevant events discussed in Section 2.3. Figure 5b shows the same integrated variables for the second simulation, covering a larger time-span. The vertical gray lines represent the time-span of the first simulation. Figure 5c shows the average values of temperature and velocity for the filament in the large time-span simulation.

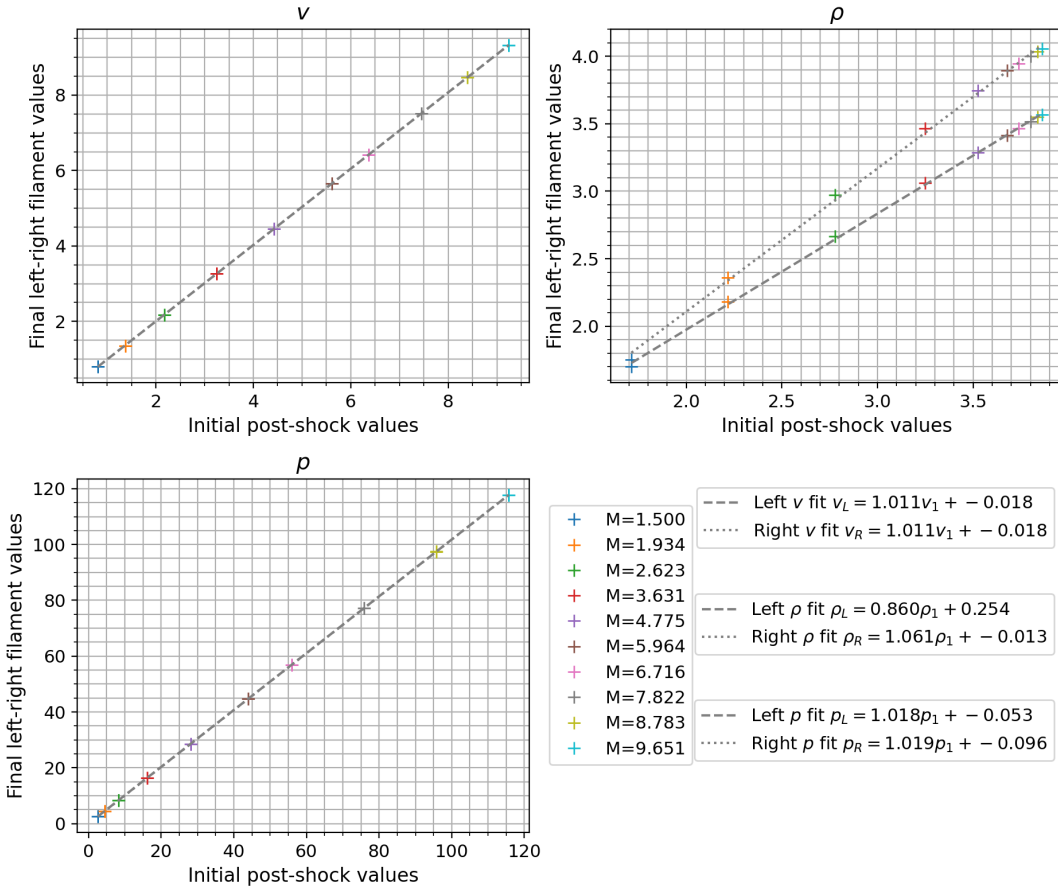


Figure 6: Comparison of initial post-shock values and final values to the left and right of the prominence when stationary state is reached in simulations with different initial shock impacting the modeled prominence.

The ideal prominence studied until now, with a sharp transition with the surrounding medium, does not represent a real solar prominence. Its edge, known as the prominence-corona transition region (PCTR), does not involve a sharp transition that can be analyzed as a discontinuity problem when it is impacted by a shock. The prominence modeled in the simulations of Section 3 will not be sharp either. In order to study a more realistic situation, experiments with a smoothed prominence (with its transition represented by a sine function) were carried out. The initial perturbations produced after impact were not exactly identical to the ideal case studied above but followed the same dynamic of secondary perturbations propagating and subsequently accelerating the prominence. The stationary state reached is the same in both cases, proving that even though the initial impact of the smoothed case cannot be analytically studied, the results obtained here are general.

2.5 Introduction of thermal conduction

Thermal conduction has not been considered yet, but it is an essential process that shapes the dynamics of the hot plasma in the solar corona. Thermal conduction is modeled by including in the energy equation the effect of the heat flux using the standard diffusion approximation, namely:

$$\mathbf{q} = -\kappa(T) \nabla T, \quad (2.4)$$

where $\kappa(T)$ is the diffusion coefficient. The Spitzer conductivity [Spitzer 1962] will be used, with $\kappa(T) = \chi \cdot T^{5/2}$, where χ is the Spitzer conduction coefficient with a value of $8 \cdot 10^{-7} \text{ g cm s}^{-3} \text{ K}^{-7/2}$, a typical value for coronal regions that is set in the AMRVAC code. In the 1D situation of the present chapter, the temperature gradient in Eq. 2.4 is just given by the derivative with respect to x . The resulting energy equation will be:

$$\partial_t e + \nabla \cdot (\mathbf{v} e) = -p \operatorname{div} \mathbf{v} - \operatorname{div} \mathbf{q}, \quad (2.5)$$

with e the internal energy density per unit volume, \mathbf{v} the velocity vector, p the pressure and \mathbf{q} the heat flux. We see that the latter appears in the energy equation through a term of the form $-\operatorname{div} \mathbf{q}$. The characteristic time of thermal conduction for a given physical state with values of internal energy per unit volume, temperature and characteristic length scale e_0 , T_0 and L_0 , respectively, will be given by:

$$\tau_{TC} = \frac{e_0}{\kappa_0 T_0 / L_0^2} = \frac{p_0 / (\gamma - 1)}{\chi T_0^{7/2} / L_0^2}, \quad (2.6)$$

with $\kappa_0 = \chi T_0^{5/2}$. In contrast to the above simulations, thermal conduction (and radiative cooling further along) impose their own timescales on the calculation, given by the physical properties of the coronal medium. Thus we are no longer free to choose arbitrary units. The units we are using are defined in Appendix A.

The effect of thermal conduction on a shock wave was studied by Zel'dovich and Raizer 1967 and Lacey 1988. The authors concluded that the temperature profile cannot be discontinuous across the shock, given that any jump in temperature would lead to an unphysical infinity in the heat flux deposition (mathematically: the temperature appears in a second-order derivative in the conduction term in the energy equation). There is still the possibility of a jump in pressure, density and velocity, like in standard shocks, but, for that, the shock must be strong enough. Also interesting, the presence of heat conduction leads to a *thermal precursor*, i.e., a region of enhanced temperature in the pre-shocked domain that announces to the unshocked gas that a shock is about to reach it.

Neither Zel'dovich and Raizer 1967 nor Lacey 1988 presented actual solutions to the equations

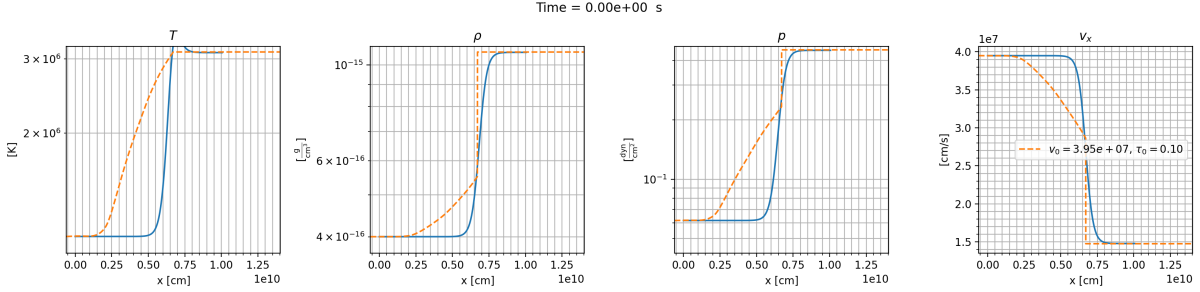


Figure 7: Numerical test to validate the predicted shock-profiles under thermal conduction by Lacey 1988. The blue lines represent the initial conditions of the simulation, while the orange dashed lines represent the theoretical expected profile for the shock propagating to the left in the frame of reference at rest with it. The theoretical profile is naturally reached after ~ 500 s, shown in [Video 3](#).

describing a shock with non-zero thermal conduction, but we need them. In order to obtain the physical profiles, Appendix B contains a detailed derivation of the equations to be solved together with discussion of the solutions. As seen in the appendix, the solution for the shock profiles can be obtained by integrating an ordinary differential equation in terms of dimensionless variables with a single regulating parameter, namely, $\tau_0 = (p_0/\rho_0)/v_0^2$ constructed with the pre-shock values of pressure, density and fluid velocity in a system of reference at rest with the shock front. For any value of τ_0 there will be infinite self-similar solutions that depend only on the dimensionalization of variables. Further, as solutions of his equations Lacey 1988 discussed cases with actual shock shape of the type explained in the previous paragraph (i.e., with jumps in p , ρ and v but not in T), as well as smooth transitions where the increase of density and pressure is not sufficient to lead to an abrupt transition in them. An example of the two different types of spatial profiles is shown in Figure 18.

An important question is whether the Lacey solutions are really attainable in an actual physical system. To prove so, we developed a simple simulation. A smooth step-like profile was modeled by a hyperbolic tangent function. The jumps respect the predicted values by the theory of shocks under thermal conduction described by the authors, so that the expected solution is a shock that will remain static in this frame of reference with fluid incoming from the right contour. Figure 7 illustrates the initial conditions in blue lines, while the expected theoretical profile is shown in orange dashed lines. The evolution of the simulation is available in [Video 3](#)⁴. It can be seen that the smooth profile suffers some oscillations due to the perturbations created by the difference from the natural profile it should have. After $t \approx 500$ seconds, the numerical solution adapts to the expected theoretical profile. The time required matches the characteristic conduction time obtained for the pre-shock state from Eq. 2.6, $\tau_{TC} \approx 600$ s.

Further tests of these thermal conduction shock profiles are performed in Section 2.6.

2.6 Impulsive heating perturbation

A different experiment was carried out in preparation of the perturbation generation mechanism used in the 2D simulations of Chapter 3. It consisted in a homogeneous initial state that gets perturbed by localized impulsive heating for an interval of time. This heating leads to an increase in the entropy, internal energy and pressure which generates propagating perturbations of explosive nature traveling to the left and right, while a third perturbation remains static in the center. These calculations were performed with thermal conduction and radiative cooling activated. The AMRVAC code implements optically thin radiative cooling that describes locally the energy loss by radiation $Q_{rc} = n_i n_e \Lambda(T)$, where

⁴https://drive.google.com/file/d/14sPCt1DreHKHNQcpCip_yxrhemvnYkDl/view?usp=share_link

n_i and n_e are the ion and electron number densities and $\Lambda(T)$ is the cooling function or curve that represents the efficiency. In the present work we implemented the original table by Colgan et al. 2008.

To model the impulsive heating we have to increase the entropy of the system in a limited spatial range. To that end the internal energy is increased with a spatial Gaussian profile in that range without modifying the mass density. More in detail, the Gaussian is centered at x_0 and has a full-width at half-maximum of σ_x . The impulsive heating is modeled in three phases: a linear increase of the heating for one fourth of the total duration of the impulse, constant heating with maximum value for one half of the duration and a final linear decrease for one fourth of the time.

We have carried out an experiment with impulsive heating in the center of the spatial domain lasting for 100 seconds. The results can be viewed in [Video 4⁵](#). The internal energy excess can be clearly seen in the center of the domain which leads to two shock-like perturbations propagating to the left and right. Figure 8 helps analyze the experiment. Figure 8a shows a snapshot of the state of the system when the propagating perturbations have almost detached from the remaining central perturbation. The latter is the equivalent here of the entropy mode in the elementary theory of sound waves.

Figure 8b contains the x position of the shock front propagating to the right as a function of time in the first panel. The position is calculated by locating the point with the maximum slope in pressure. A linear fit is shown as a black dashed line, allowing to obtain the mean propagation speed of the shock front. The corresponding dimensionless value $\tau_0 = (p_0/\rho_0)/v_0^2$, relevant to obtain the theoretical shock profile in the following, can be computed with the pre-shock values of pressure and density and using for v_0 the shock propagation speed. The second panel shows the instantaneous velocity of the shock front, calculated with centered finite differences with an 11-point stencil. It can be seen that the instantaneous propagation speed decreases with time, leading to an increasing value of τ_0 as the shock advances. The deceleration of the perturbation could be expected, because, when the impulsive heating perturbation has finished, there is no further energy input into the system whereas the propagating perturbation is constantly transferring energy to the unshocked medium in its way.

There are two points marked in Figure 8b in orange and green color respectively. The fluid state at these instants of time is represented as blue lines in 8c and 8d, while the expected theoretical profile is represented with orange and green lines for each instant of time. Both figures include the temperature, density, pressure and velocity profiles zoomed around the shock front propagating to the right. It can be seen that the perturbation profile resembles the thermal conduction profiles described by Lacey 1988 and explained in Section 2.5 and Appendix B, with a smooth change in temperature and a thermal precursor followed by jumps in all other variables. The theoretical profile computed with the corresponding instantaneous τ_0 is superimposed over the simulation results in orange and green for each instant of time. The relative error between simulation and theoretical result is calculated for points enclosed between the vertical black dotted lines and is displayed below each profile. Comparing both instants of time, it can be seen that the similarity between the numerical and theoretical results improves with time as the perturbation gradually reaches the asymptotic shape prescribed by the equations.

⁵https://drive.google.com/file/d/1EJnD71-LyOpPODwUnXzhDItyB5FnNfJJ/view?usp=share_link

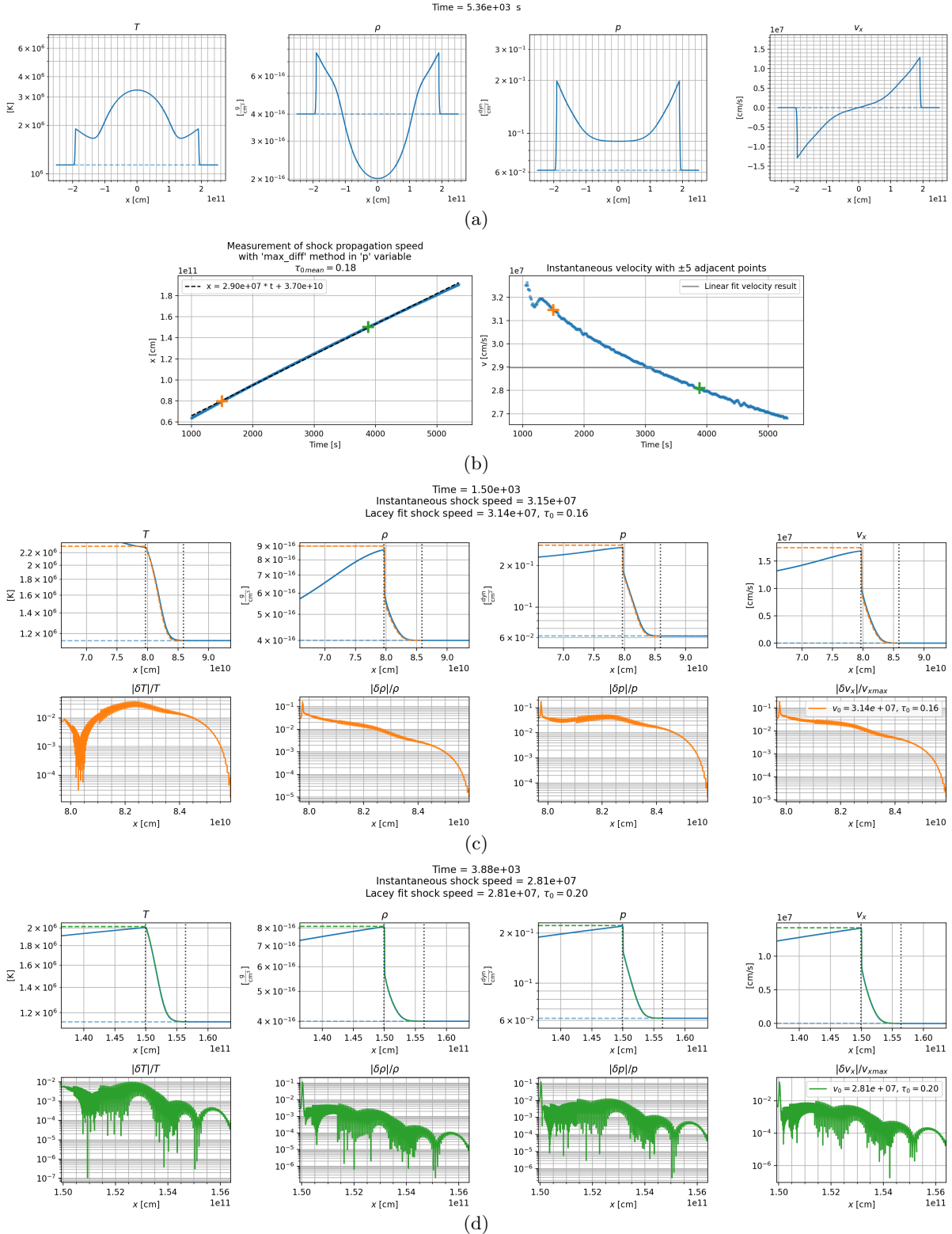


Figure 8: Localized impulsive heating simulation. 8a represents the fluid state at an instant of time when shock perturbations have separated from the central static perturbation. A video animation of the simulation can be seen in [Video 4](#). 8b represents the time evolution of position of the rightwards shock front and a linear fit with the average velocity in the left panel, and the instantaneous propagation velocity in the right panel. Two instants of time are marked, and their profiles are compared to the expected theoretical profiles in 8c and 8d.

3 Two-dimensional simulations

In the previous Section (2), the impact of shock fronts on prominence-like structures (denser and cooler fluid) has been extensively studied in an idealized 1D scenario. These simulations considered the effects of thermal conduction and radiative cooling on the propagation of the shock perturbations. In this section, we consider a much more realistic two-dimensional configuration with a dipped magnetic field and the process of formation of solar prominences by the Thermal Non-Equilibrium process (TNE; Antiochos and Klimchuk 1991; Karpen et al. 2005; Keppens and Xia 2014). This process is also called the evaporation-condensation mechanism (see Sect. 3.1.2).

The simulation set-up consists of a two-dimensional Cartesian grid that spans $2 \cdot 10^{10}$ cm (200 Mm) in the horizontal direction and 10^{10} cm in the vertical direction. The numerical domain has an initial resolution of 96 grid points in the horizontal direction and 48 in the vertical direction, while the adaptive grid refinement (AMR) is performed up to level five. This means that spatial resolution is increased by a factor $2^4 = 16$ with an equivalent grid size of 1536×768 , which allows to resolve lengths of $130\text{ km} \times 130\text{ km}$. Thermal conduction and radiative cooling are applied as explained in Sections 2.5 and 2.6. The simulation consists of three different phases, which are listed below and explained in detail in the following sections:

1. The prominence is formed in a self-consistent way by the evaporation-condensation process in a potential magnetic field configuration with a dipped region.
2. Once the prominence has formed in the dipped region, the impulsive heating phase begins. By increasing internal energy in a footpoint of the field lines holding the filament, a shock-like perturbation is created. This perturbation propagates along the field lines until it impacts the filament.
3. The final phase of the simulation is dedicated to the study of the prominence motion after the impact of the perturbation. Oscillations at different heights are measured and compared.

The main tools for analyzing results in the present Section will consist of the two-dimensional plots of different variables, their profiles along some indicated field lines, and the space-time plots obtained from the one-dimensional profiles along one of the field lines. Various video animations will be provided, the ones labeled *a* will contain two-dimensional maps and the ones labeled *b* will contain the one-dimensional profiles along the specified field lines.

3.1 Prominence formation

3.1.1 Initial conditions

The initial temperature follows a piecewise function that defines the chromosphere, the transition region, and the corona. For heights below $2 \cdot 10^8$ cm, the temperature profile is defined by:

$$T(y) = T_{\text{chr}} + \frac{1}{2} (T_{\text{top}} - T_{\text{chr}}) \left[1 + \tanh \left(\frac{y - h_{\text{tra}} - 27 \times 10^6}{w_{\text{tra}}} \right) \right], \quad (3.1)$$

being $T_{\text{chr}} = 8 \cdot 10^3$ K the temperature at the base of the chromosphere, $T_{\text{top}} = 1.5 \cdot 10^6$ K the temperature at the top of the corona, $h_{\text{tra}} = 2 \cdot 10^8$ cm the height of the transition region and $w_{\text{tra}} = 2 \cdot 10^7$ cm the width of the transition region. For positions above the transition region h_{tra} , the temperature is defined as:

$$T(y) = \left(3.5 \frac{F_{\text{cond}}}{\kappa} (y - h_{\text{tra}}) + T_{\text{tra}}^{7/2} \right)^{2/7}, \quad (3.2)$$

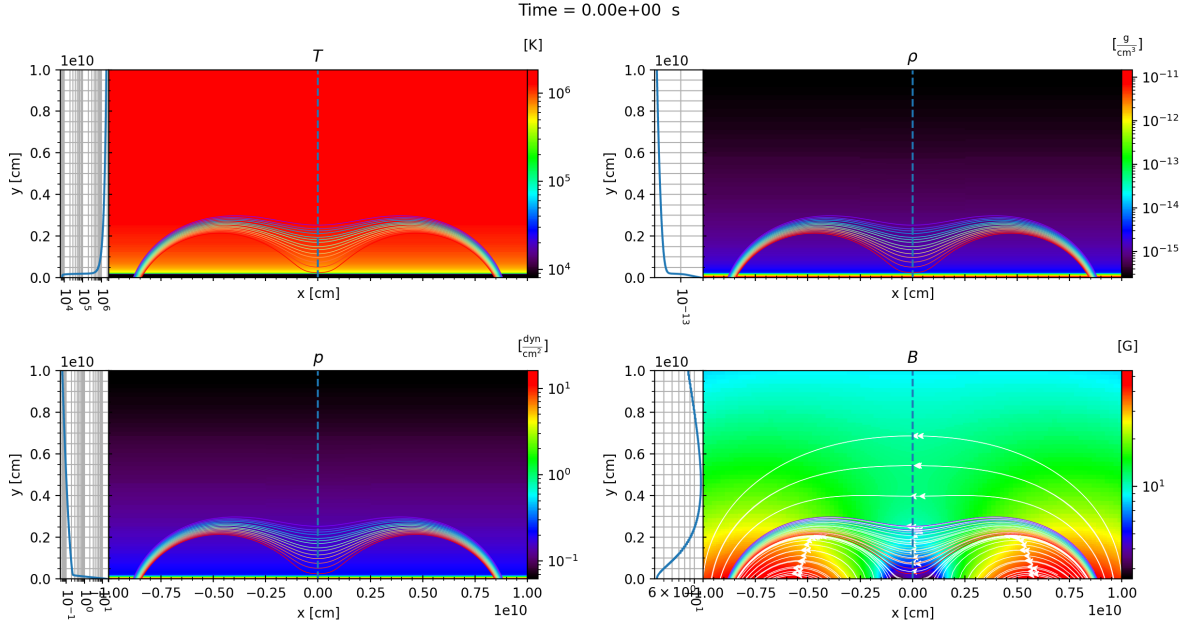


Figure 9: Initial conditions for the 2D simulation, showing temperature, density, pressure and total magnetic field. A vertical profile at $x = 0$ is shown to the left of every map. A set of 14 field lines are represented in rainbow colors and they will be used to study the physical phenomena of interest.

where $F_{\text{cond}} = 2 \cdot 10^5 \text{ g s}^{-3}$ is the constant thermal conduction flux, $\kappa = 8 \cdot 10^{-7} \text{ g cm s}^{-3} \text{ K}^{-7/2}$, $h_{\text{tra}} = 2 \cdot 10^8 \text{ cm}$ the height of the transition region and $T_{\text{tra}} = 1.6 \cdot 10^5 \text{ K}$ the upper temperature of the transition region. This expression is derived from considering thermal conduction equilibrium. The density and pressure profiles are calculated so that hydrostatic equilibrium is achieved, with electron number-density in the chromosphere $n_{\text{chr}} = 1.15 \cdot 10^{15} \text{ cm}^{-3}$. The initial condition maps of temperature, density and pressure are displayed in Figure 9. A vertical profile at $x = 0$ is shown to the left of each panel, where the different functions for the chromosphere, transition region and corona can be distinguished.

Different magnetic field configurations have been proposed to explain the support of solar filaments against gravity (see e.g. Mackay et al. 2010). In the present work, we have chosen a quadrupolar magnetic field configuration. It consists of the combination of three dipoles centered at $x = -60, 0$ and 60 Mm , with the central dipole having an intensity that is 0.23 times that of the lateral ones. Their combination produces a dipped region in the magnetic field at the center of the horizontal axis. The magnetic field configuration is shown in Figure 9 (lower right panel). The color map represents the total magnetic field intensity. A set of 14 field lines, displayed in rainbow colors, is plotted; these field lines will be used throughout the present work to study the physical phenomena of interest. In addition, extra field lines are drawn in white to better illustrate the global structure of the magnetic field.

3.1.2 Simulation evolution

Nowadays, it is thought that the origin of the filament mass is the chromosphere. This mass evaporates from the chromosphere, travels along the magnetic field lines, and condenses in the dips of the magnetic structure. This is the so-called evaporation-condensation mechanism. This process requires the dominant heating to be localized in the lower layers of the corona, a condition that is supported by observational evidence. However, the nature of this heating is not known and is usually imposed by a function $H = H(x, y)$. The heating has two components, the background heating and the localized heating, $H =$

$H_{\text{bck}} + H_{\text{loc}}$, both included in the MHD energy equation:

$$\partial_t \epsilon + \nabla \cdot (\mathbf{v} \epsilon - \mathbf{B} \mathbf{B} \cdot \mathbf{v} + \mathbf{v} p_{\text{tot}}) = \nabla \cdot (\mathbf{B} \times \eta \mathbf{J}) - Q_{rc} - \mathbf{\text{div}} \mathbf{q} + H, \quad (3.3)$$

where ϵ is the total energy density, \mathbf{v} the velocity vector, \mathbf{B} the magnetic field, p_{tot} the total pressure, η the resistivity, \mathbf{J} the current density vector, Q_{rc} the radiative loss and \mathbf{q} the heat flux. The background heating is used to maintain the solar atmosphere in equilibrium, compensating for the energy losses due to radiation and conduction. Without this heating, the atmosphere would cool down in less than one hour.

Numerous one-dimensional numerical simulations have been conducted (e.g., Karpen et al. 2005; Luna et al. 2012b). More recently, multi-dimensional simulations have also become feasible thanks to the capabilities of the new numerical codes (e.g., Xia et al. 2012). The numerical setup closely resembles that used by Zhou et al. 2023, especially in the way the coronal heating is implemented. The background heating follows a vertically decaying exponential profile, with a very slow decrease with height characterized by a scale height of $\lambda_{\text{bck}} = 50$ Mm. The expression is shown in Eq. 3.4, with $H_{\text{bck},0} = 6 \times 10^{-5}$ erg cm $^{-3}$ s. In contrast, the localized heating decreases much more rapidly with height from the transition region ($h_{\text{tra}} = 2$ Mm), with a characteristic scale height of $\lambda_{\text{loc}} = 10$ Mm. Horizontally, it is a gaussian profile centered at $x_1 = -8.6 \cdot 10^9$ cm and $x_2 = 8.6 \cdot 10^9$ cm and with $\sigma_{\text{loc}} = 3$ Mm in order to heat a specific bundle of field lines. The expression is shown in Eq. 3.5, with $H_{\text{loc},0} = 5 \times 10^{-2}$ erg cm $^{-3}$ s $^{-1}$.

$$H_{\text{bck}}(x, y) = H_{\text{bck},0} e^{-\frac{y}{\lambda_{\text{bck}}}}, \quad (3.4)$$

$$H_{\text{loc}}(x, y, t) = H_{\text{loc},0} \left[e^{-\frac{(x-x_1)^2}{\sigma_{\text{loc}}^2}} + e^{-\frac{(x-x_2)^2}{\sigma_{\text{loc}}^2}} \right] e^{-\frac{(y-h_{\text{tra}})^2}{\lambda_{\text{loc}}^2}}. \quad (3.5)$$

In the following paragraphs the initial evolution of the simulation will be analyzed. Video 5a⁶ presents the evolution of the two-dimensional maps of temperature, density, pressure, velocity parallel and perpendicular to the magnetic field and the plasma β parameter. The initial condition is shown in Figure 9 and the an advance snapshot at $t = 93$ minutes, after the prominence is created, is shown in Figure 10a.

The formation of the filament takes place because the localized heating evaporates plasma from the chromosphere, which then accumulates in the dipped region of the magnetic field, where it condensates. The condensed prominence mass can be appreciated in both temperature and density maps as a region two orders of magnitude colder and denser. Two velocity maps are added, containing v_{\parallel} and v_{\perp} . The fluid velocity parallel to the magnetic field v_{\parallel} is defined antiparallel to the magnetic field $\vec{v}_{\parallel} = -\vec{v} \cdot \vec{B}/|\vec{B}|$. This criteria is chosen because the magnetic field has $B_x < 0$ in the whole domain but it is intuitive to have $v_{\parallel} > 0$ where $v_x > 0$, i.e., when fluid motion goes from left to right footpoint. The perpendicular velocity v_{\perp} is defined to have the general sign of v_y , i.e., positive when fluid motion is directed upwards. From the parallel velocity plot it can be seen how the chromospheric plasma is being brought upwards through the field lines (evaporation) to the dipped region (red flow to the left of the prominence, blue flow to the right), where it becomes part of the filament (condensation). The perpendicular velocity (much lower than the parallel velocity) shows the propagation of Alfvénic waves, perturbations in v_{\perp} that propagate along the magnetic field lines. The available animation shows considerable noise in v_{\perp} at the beginning of the simulation. This is due to the propagation and reflection of Alfvénic waves in the domain contours, until they dissipate. These initial perturbations are due to the

⁶https://drive.google.com/file/d/1kka0UE94GT3jIRq8RTL4hc90byaHmc1-/view?usp=share_link

un-relaxed initial conditions, but they are not dynamically relevant due to their low amplitude. Figure 10a (bottom right) displays the parameter $\beta = p_{\text{gas}}/p_{\text{mag}}$. Its value remains clearly below 1 along the entire set of selected field lines; a magenta contour at $\beta = 0.1$ is also plotted, delimiting a low height region quite close to the chromosphere.

The different field lines over-plotted in rainbow colors are used to study the profiles along them, as it can be seen that $\beta << 1$ throughout the set of lines and motion can be considered purely along the field lines. The animation evolution of the same variables along the profiles of the field lines can be seen in [Video 5b⁷](#), where plasma motion towards the center is clear in the v_{\parallel} plot and sudden condensation in the central region can be appreciated in the T and ρ plots.

Figure 10b represents the space-time plot along one of the central field lines, with footprint at $x_0 = -8.58 \cdot 10^9$ cm and height of the dip at $y_{\text{dip}} = 1.35 \cdot 10^9$ cm. This field line, centered in the impulsive heating region, will be used further along to analyze the dynamics of the simulation. The vertical axis in the plots represents the arc-length distance along the field line (beginning at the left footprint), and the horizontal axis represents the time. The plot is zoomed to the central region of the field line and to the moment of time when condensation happens at this height, namely $t \approx 3000$ s and $s \approx 9.8 \cdot 10^9$ cm. From the temperature and density plots it can be appreciated how plasma condensation happens suddenly. From the longitudinal velocity and pressure plots, it can be seen that two rarefaction waves are created when the plasma condenses and propagate towards the left and right footpoints. The Alfvénic waves propagating along the field line are visible in the v_{\perp} plot. All these perturbations are associated with thermal instability leading to condensation.

3.2 Impulsive heating, propagation and impact

3.2.1 Impulsive heating set-up

Following the example detailed in Section 2.6, an additional source term increases the internal energy in a localized region at a given time. This excess pressure generates a coronal wave that transports energy along the field lines. This setup aims to mimic the event described by [Luna et al. 2024](#). Due to the short duration and abrupt energy increase, the resulting wave is a shock. This method of introducing external perturbations affecting prominences has been applied in several studies ([Liakh et al. 2020](#), [Liakh et al. 2023](#), [Jerčić et al. 2022](#)).

The impulsive heating consists in an extra term in the localized term of Eq. 3.3 as $H = H_{\text{bck}} + H_{\text{loc}} + H_{\text{imp}}$. The extra term H_{imp} is only applied at the left footpoint. This is applied over an 85 s interval, from $t = 6440$ s to 6525 s. During the first quarter the heating increases linearly, then it stays constant for half of the total time and during the last quarter it decreases linearly. The initial amplitude will be $Q_0 = 5 \cdot 10^{-2} \text{ kg m}^{-1} \text{ s}^{-3}$, with the left-side increasing its amplitude by a factor of 30.

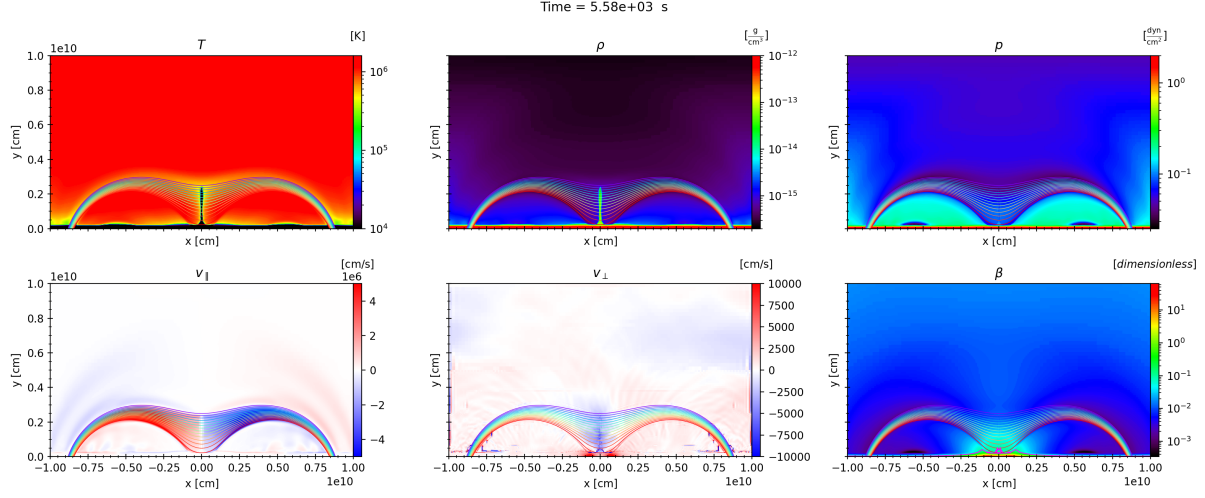
3.2.2 Perturbation propagation

At $t = 6440$ s = 107.3 min the impulsive heating begins. Two video animations are available here: [Video 6a⁸](#) and [Video 6b⁹](#). The first animation shows the two-dimensional maps, where the sudden increase of internal energy at the left footpoint causes a density, pressure and velocity perturbation that propagates along the field lines towards the dipped region where the prominence is held. The second animation illustrates the evolution of the profiles along the field lines, allowing to identify the evolution of the perturbation into a shock that propagates along the field lines until the moment of impact.

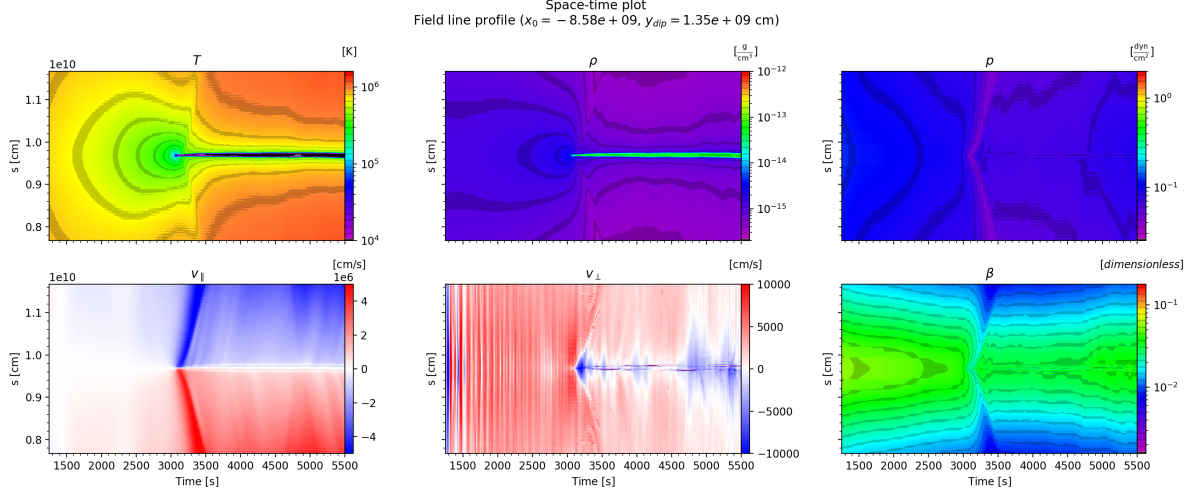
⁷https://drive.google.com/file/d/1lqTQrpg08fk_f600JaRRa2dM6JJU0znN/view?usp=share_link

⁸https://drive.google.com/file/d/1oxpc4a_VWtX4RQBbP6eJz0_dRg_88t__/view?usp=share_link

⁹https://drive.google.com/file/d/1elzUNim2ZL3_q0Yj1E9YrNoxmS7DegId/view?usp=share_link



(a) Simulation snapshot after prominence is formed. It can be seen that the colder and denser prominence mass is in pressure equilibrium. The parallel velocity map shows the flow of chromospheric material to the filament, while the perpendicular velocity map shows the propagation of Alfvén waves along field lines. The β map has a magenta contour of $\beta = 0.1$ over-plotted. The animation corresponding to this plot is available in [Video 5a](#).



(b) Space-time plot of one of the field lines with footpoint at $x_0 = -8.58 \cdot 10^9$ cm and height of the dip $y_{dip} = 1.35 \cdot 10^9$ cm. The vertical axis represents the arc-length distance along the field line (beginning at the left footpoint) and the horizontal axis the time. The plot is zoomed to the moment of condensation in the central region of this line.

Figure 10

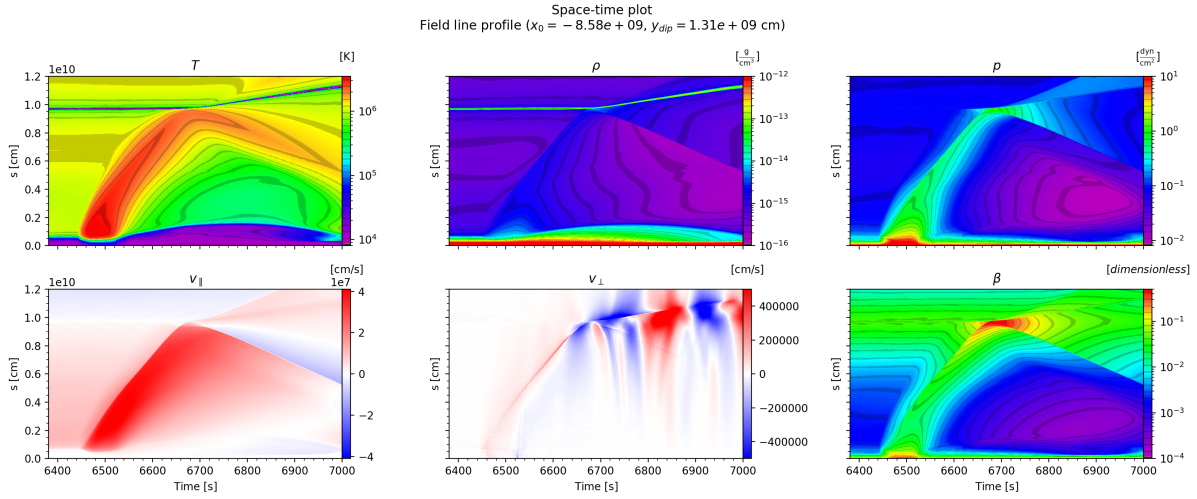
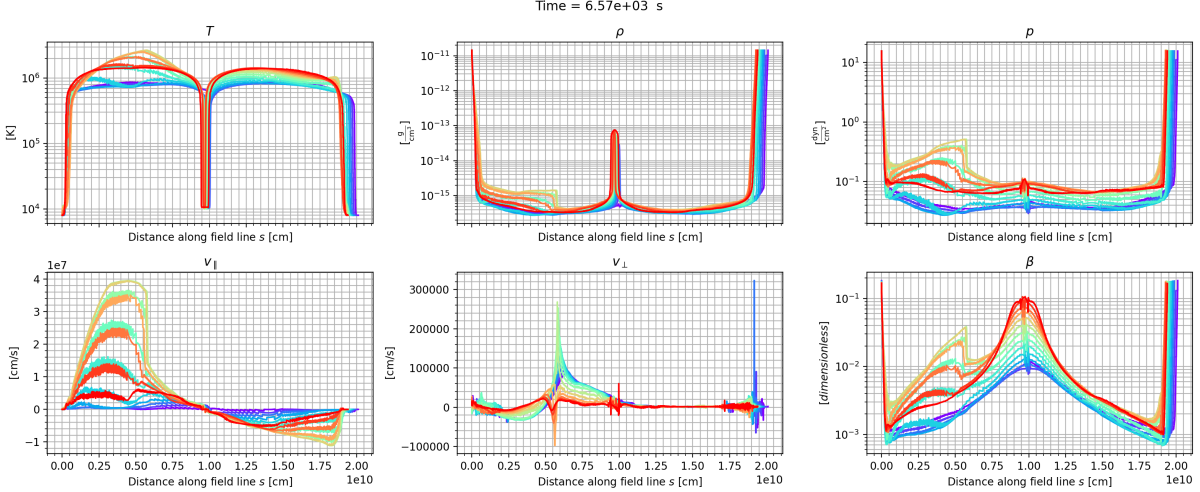


Figure 11: Space-time plot of the profile along the field line centered at the impulsive heating region, with footpoint $x_0 = -8.58 \cdot 10^9$ cm and height of the dip at $y_{dip} = 1.35 \cdot 10^9$ cm. The plot is zoomed to the moment of impulsive heating and the path covered by the perturbation until impact.

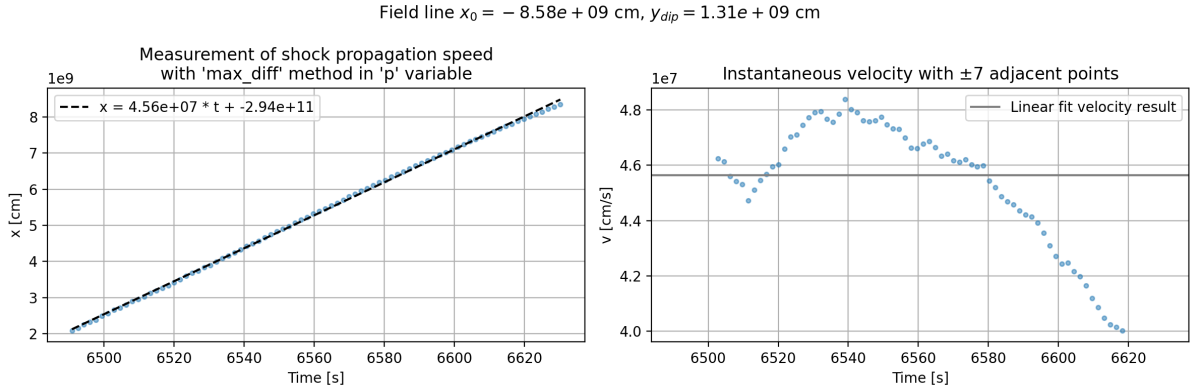
Figure 11 shows the space-time diagrams along the selected central field line of the generation and propagation of the shock, and its impact on the prominence. To create the diagrams, the quantities along the previously chosen field line centered at the impulsive heating maximum are represented versus the arc-length along the field line. Around $t_0 = 6450$ s, the heating effects become noticeable, and a perturbation begins to propagate towards the center of the field line. The prominence mass is visible as a cold and dense region located at $s = 9.8 \cdot 10^9$ cm. At approximately $t_1 = 6650$ s, the perturbation reaches the filament. Its propagation will be clearly analyzed in Figure 12. The impact of the perturbation on the prominence is clearly visible in all the panels of Figure 11. In the end of Video 6a and in the temperature plot of the previous figure it can be seen that the thermal precursor (detailed below) reaches the perturbation, and pressure begins increasing, but it is not until the pressure jump impacts the cold mass that it is set into motion. As studied in the one-dimensional experiments of Section 2, the perturbation will partly transmit across the filament and partly reflect (visible in the v_{\parallel} space-time map), transmitting momentum to it. The secondary reflecting perturbations will not be studied in detail, but the prominence motion will be explained in the following section. Regarding the impact, it can be seen in the pressure space-time map that the sudden pressure increase causes a peak value of $\beta = 0.6$, but the pressure is released and β is lowered again when motion begins. The v_{\perp} space-time map shows the magnetosonic waves that propagate through the field line and continuously affect the prominence.

The profiles along a specific set of field lines are analyzed to investigate in detail the perturbation and its propagation. Figure 12a shows a snapshot of the available Video 6b, displaying the profiles along the different field lines over-plotted in figures as 10a. The prominence can be distinguished as the cold and dense region around $s = 10^{10}$ cm. There is a slight shift in its position among the different field lines because the total length of the field lines varies, but the filament is always in the middle of it. The perturbation is clearly visible to the left side of the prominence. As seen in the one-dimensional case in the previous Section 2.5, the existence of a thermal precursor can also be observed in two dimensions. The temperature profile is smooth and density, pressure and velocity present jumps (around $s = 6 \cdot 10^9$ cm) that are preceded by a smooth growth.

With the purpose of improving the characterization of the perturbation, Figure 12b displays the measurement of the shock propagation speed along the field line at the center of the impulsive heating region. The left panel displays the position of the shock front, located by identifying the point with



(a) The lines are color-coded to indicate the different field lines, with the color scheme shown in Figure 10a. Profiles along the different field lines under analysis are displayed. The shock-like perturbation generated by the impulsive heating can be seen propagating from the left toward the prominence located at the center.



(b) Measurement of the shock propagation speed along the field line at the center of the impulsive heating region. The left panel shows the position detected for the shock front by locating the point with maximum slope in pressure. A linear fit shows the average propagation velocity. The right panel shows the instantaneous velocity calculated at each time by considering the position of the shock only in the seven past and future instants.

Figure 12

greatest slope in pressure. A linear fit with mean velocity $v_{prop} = 4.56 \cdot 10^7 \text{ cm/s} = 456 \text{ km/s}$ is obtained. The right panel contains the instantaneous velocity of the shock front, calculated at each instant with centered finite differences with a 15-point stencil, i.e., the 7 past and future instants of time. It can be seen that the shock propagation velocity increases during the first 40 seconds, and then decreases. The shock speed is expected to vary initially due to the inhomogeneous conditions of the medium it travels through as it climbs up to the corona. Then the energy loss during propagation is expected to slow down the perturbation, as there is no constant force pushing from behind the shock.

A calculation of the sound speed and the Alfvén speed in the path followed by the shock yields $c_{s,max} \approx 2 \cdot 10^7 \text{ cm s}^{-1}$ and $v_{A,max} = 4 \cdot 10^8 \text{ cm s}^{-1}$, so the propagating perturbation has a sonic Mach value of $M_s = 2.3$. Focusing on the central field line (the one with greatest jumps in 12a, whose space-time plot is shown in 11), the temperature grows from $T \approx 10^6 \text{ K}$ in the corona to $T \approx 3 \cdot 10^6 \text{ K}$ in the shocked medium, while density and pressure jump from $4 \cdot 10^{-16} \text{ g cm}^{-3}$ and 0.08 dyn cm^{-2} to $1.5 \cdot 10^{-15} \text{ gm cm}^{-3}$ and 0.5 dyn cm^{-2} respectively, rendering a density jump of 3.75 and a pressure jump of 6.25. Velocity

	T	ρ	p	u
Measured jumps	3.00	3.75	6.25	0.28
Theoretical jumps	2.73	2.67	7.30	0.67
Non TC jumps	2.49	2.55	6.36	0.61

Table 2: Comparison of measured jumps, expected theoretical jumps for a shock-front with $\tau_0 = p_0/\rho_0/v_{prop}^2 = 0.1$ (jump relations (B.17)-(B.20)) and expected theoretical jumps for a hydrodynamical shock with no thermal conduction (TC) and $M_s = 2.3$ (jump relations (2.1)-(2.3)).

jumps from 10^7 cm s^{-1} in the pre-shock medium to $3.6 \cdot 10^7 \text{ cm s}^{-1}$, rendering a velocity jump of 0.28 in the reference system moving at $v_{prop} = 4.6 \cdot 10 \text{ cm s}^{-1}$, where the shock-front is static. These results are summarized in Table 2, where the obtained jumps are compared to those expected for a shock front propagating with the measured velocity through a homogeneous medium with the pre-shock density and pressure. As explained in Section 2.5 and Appendix B, the jump will be characterized by the parameter $\tau_0 = p_0/\rho_0/v_{prop}^2 = 0.1$ and the jump relations are given in Eqs. B.17-B.20. The table also shows the expected jumps for a hydrodynamical shock with no thermal conduction that propagates through the homogeneous medium ρ_0, p_0 with $M_s = 2.3$, calculated with Eqs. 2.1-2.3.

The results presented in Table 2 do not match the ideal hydrodynamical jumps nor the expected jumps for thermal conduction profiles. This discrepancy is due to the inhomogeneous pre-shock medium and the short propagation distance, which does not allow sufficient time for the perturbation to fully develop its natural shock shape. The attempt to fit the obtained profile to the theoretical expectations does not provide a satisfactory agreement. A secondary test using the same 2D setup and the same impulsive heating, but without the prominence formation, is presented in Appendix C. In this case, **a very good agreement between the obtained perturbation and the theoretical profiles is found** when the propagation path is more homogeneous.

3.3 Prominence oscillations

After impact, the prominence mass acquires momentum (without a substantial increase in internal energy, as concluded in Section 2.4) and starts moving along the magnetic field lines ($\beta \ll 1$). This part of the simulation can be seen in Video 7a¹⁰ and Video 7b¹¹. It elongates up to a maximum displacement of $2 \cdot 10^9 \text{ cm}$ before being pulled back, initiating an oscillatory motion. The pendulum model described by Luna and Karpen 2012 and Luna et al. 2012a and further developed by Luna et al. 2016 will be applied to compare its theoretical predictions with the measured oscillation periods. In this model, the restoring force has two components: gravity projected along the magnetic field lines and the gas pressure gradient. For this reason, these oscillations are also referred to as slow magnetoacoustic-gravity oscillations. In prominences, the acoustic component is much smaller than the gravitational one, so the motion in the dipped part of the magnetic field resembles that of a pendulum. In this case, the period depends only on the radius of curvature of the magnetic field lines and is given by the expression

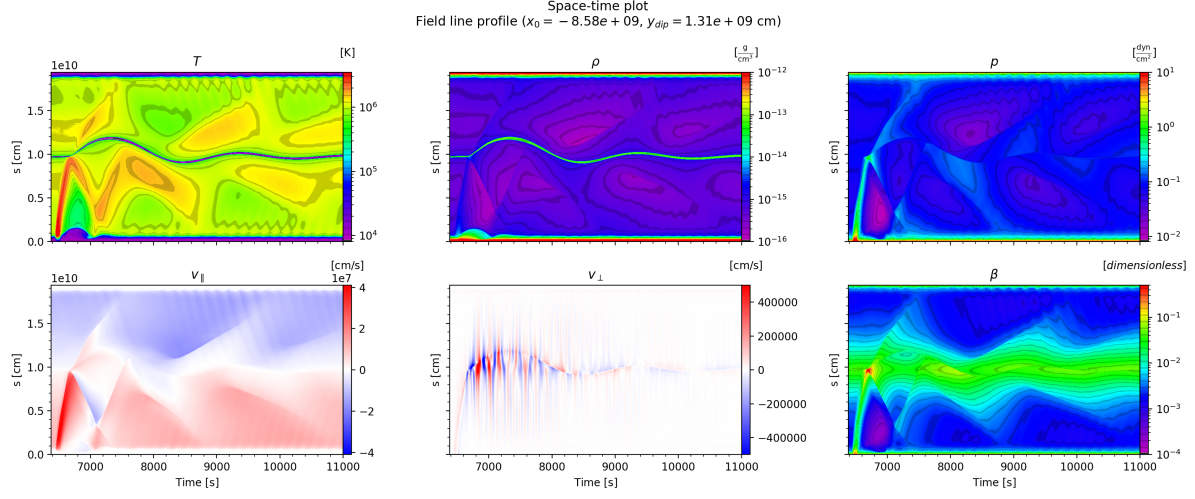
$$P = 2\pi \sqrt{\frac{R_{curv}}{g_\odot}}, \quad (3.6)$$

with R_{curv} the radius of curvature of the magnetic field line and $g_\odot = 2.74 \cdot 10^4 \text{ cm s}^{-2}$ the solar surface gravity.

Figure 13a displays the space-time map along the field line centered at the impulsive heating

¹⁰https://drive.google.com/file/d/1wGibJK-0a0hDZqdpLbFDpj6hMhUWPPED/view?usp=share_link

¹¹https://drive.google.com/file/d/1Iv8rAPC5_GAv4bcSxqxQcuFt8H5ykQ69/view?usp=share_link



(a) Space-time map of variables along the field line centered at the impulsive heating region.

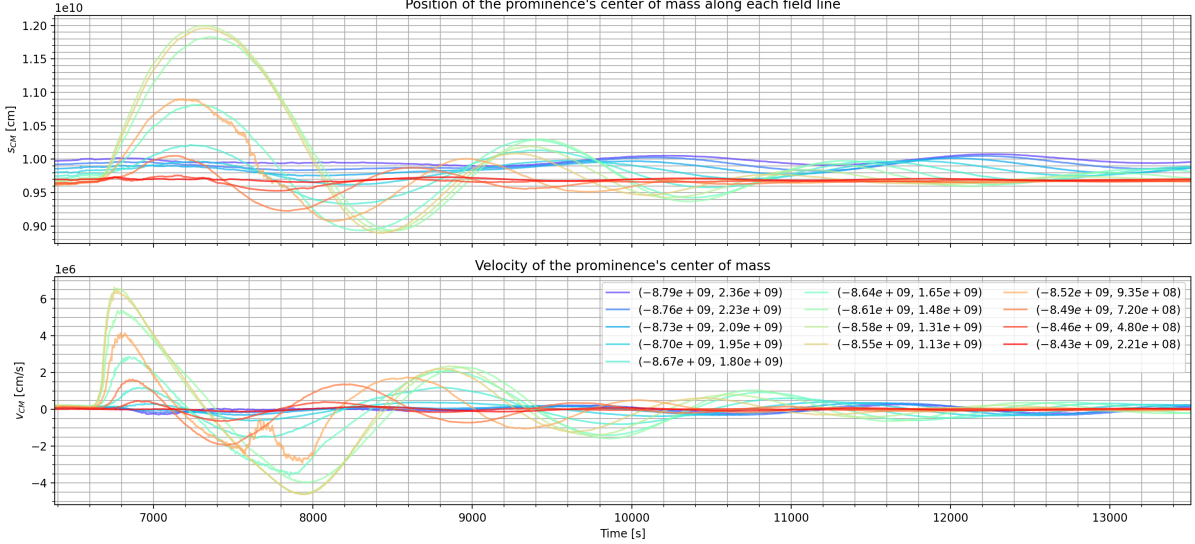
(b) Top panel displays the position of the center of mass along each field line for the entire duration of the simulation, including the impulsive heating phase. The bottom panel displays the velocity of the center of mass. The legend identifies each field line by its (x_0, y_{dip}) pair, with values given in centimeters. Note that the actual coordinates correspond to $(x_0, 0)$ and $(0, y_{dip})$.

Figure 13

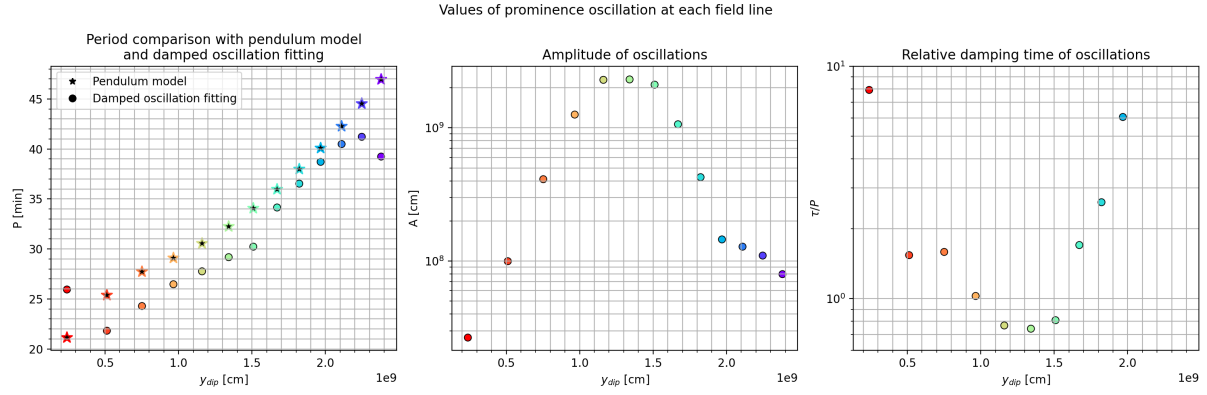


Figure 14: Results obtained for prominence oscillations through the different field lines. Period, amplitude and relative damping time of oscillation are represented versus the height of the field line dip. The theoretical pendulum model results are drawn as stars in the period plot.

region, where the oscillatory motion of the prominence is clearly visible in the temperature and density maps. The parallel velocity map shows the secondary perturbations constantly reflected between the footpoints and the filament with decreasing amplitude. The perpendicular velocity map shows the magnetosonic waves that propagate through the system. Figure 13b displays in the upper panel the evolution of the position of the center of mass of the prominence for all the field lines over-plotted in the previous 2D maps seen. The lower panel displays the velocity of the center of mass for those instants of time. The center of mass velocity is clearly above 10 km s^{-1} , confirming that we have obtained Large Amplitude Oscillation (LAO).

The simultaneous analysis of plots in Figure 13 leads to the conclusion that the filament does not initially behave as a free oscillator due to the significant influence of secondary perturbations: reflected and transmitted shocks bounce back from the footpoints, affecting the filament motion. By $t \approx 8000$, s those perturbations have decreased their amplitude and oscillations can be studied. Beyond this time, the position of the center of mass along the field line can be represented by a damped sinusoidal function, namely:

$$s = A e^{-t/\tau} \sin\left(2\pi \frac{t}{P} + \phi_0\right) + s_0. \quad (3.7)$$

Using this function, we fit the simulated motions along all the field lines under study, which yields different oscillation periods, as anticipated from the phase shifts observed among the lines in Figure 13b. The results obtained from the fitting are shown in Figure 14, where the fitted period P , the measured amplitude of elongation A , and the relative damping time τ/P are plotted as a function of the dip height.

In order to compare the measured periods with the theoretical periods given by Eq. 3.6, the radius of curvature is calculated for each field line. This calculation is performed at the dip of each line before the prominence mass condenses. Once the prominence has formed, the curvature of the magnetic field lines decreases slightly. Moreover, due to the prominence's motion, this curvature varies dynamically. However, on average, the curvature remains very similar to the value before the mass formed. This behavior occurs only under certain conditions. For very low magnetic field strengths (not usual in prominences), the field would be significantly deformed by the weight of the prominence. For completeness, theoretical periods have also been computed using the curvature measured after the prominence condensation, allowing for comparison between both estimations. Those results yield a slightly larger period (due to the lower radius of curvature) so they are not shown. The theoretical periods predicted by the pendulum model measuring the radius of curvature before the prominence condensates are represented

Velocity amplitude (km/s)	Period (min)	τ/P	Amplitude (Mm)
20 - 60	25 - 43	0.7 - 8	1-10

Table 3: Oscillation results from Figure 14.

as stars in Figure 14.

Figure 14 shows that the pendulum model predicts slightly longer periods than those observed in the simulations, but captures the variation of the period with the radius of curvature (i.e., with the height of the dip of the field line). Regarding the amplitude variation with height, it can be seen that the central field lines present the maximum elongation. This result is expected because the impulsive heating is centered on a field line crossing the center of the prominence. The relative damping time varies considerably, ranging from 0.75 (very strong damping) to 8 (weak damping). The damping time for the highest field lines was not calculated because their motion is substantially different: they do not set into motion by direct impact of the shock, but by transmission of motion from the fluid below, having the motion of a forced oscillator instead of a damped oscillator in its initial phase similar to the findings by Liakh et al. 2021.

3.4 Comparison of 2D simulations and observations

The results described in Section 3 can be compared to other numerical experiments and observations. Regarding the shock wave generated, it has a propagation speed of $v_{prop} = 460 \text{ km s}^{-1}$, which corresponds to coronal bright fronts (EIT waves) frequently seen in observations, with velocities of $200 - 500 \text{ km s}^{-1}$ and up to 1400 km s^{-1} [Long et al. 2017]. A similar perturbation was produced by Jerčić et al. 2022 in a multi-threaded prominence oscillation simulation. Table 3 summarizes the results presented in Figure 14, based on the ranges obtained for the different field lines. These results are compared to a catalog of 196 oscillatory events compiled by Luna et al. 2018 through the analysis of six months of Global Oscillation Network Group (GONG) data during solar cycle 24. Oscillations are classified as LAO or SAO according to their velocity amplitude (stripped and shaded bins in upper row of Figure 15) or regarding the type of filament in which they appear: active region, intermediate or quiescent filaments (red, green and blue in lower row of Figure 15). The results of the current simulation (Table 3) are represented as a starred shape, covering the interval of values obtained for the different heights. It can be appreciated that the oscillatory motion produced by the present simulations matches the properties of observed LAOs.

Furthermore, the similarity between the space-time plots of Figure 13a and Figure 8 of Luna et al. 2024 (adapted here in Figure 16) is noticeable. It represents the time-distance diagram in AIA 171 Å of the prominence oscillations observed along a slit on March 15th. Bright structures between 01:10 and 02:10 UT corresponds to the impulsive phase when the oscillation is triggered. There is no visible perturbation propagating and the authors concluded that it should have temperatures above 10^6 K , making it invisible in this line. Analysis of the temperature plot in Figure 13a shows how a perturbation with $T > 10^6 \text{ K}$ triggering the prominence oscillations. If a synthetic AIA 171 Å image was produced, similarities would become evident, proving the numerical simulations' affinity with the observations of jet impact on prominences and the subsequent oscillations. Unfortunately, the generation of the synthetic images goes beyond the scope of the present Master's Thesis. Nevertheless, we want to underline the fact that, even though the perturbation obtained is a shock, the smooth temperature profile due to thermal conduction may cause it to not be noticed as such in observations.

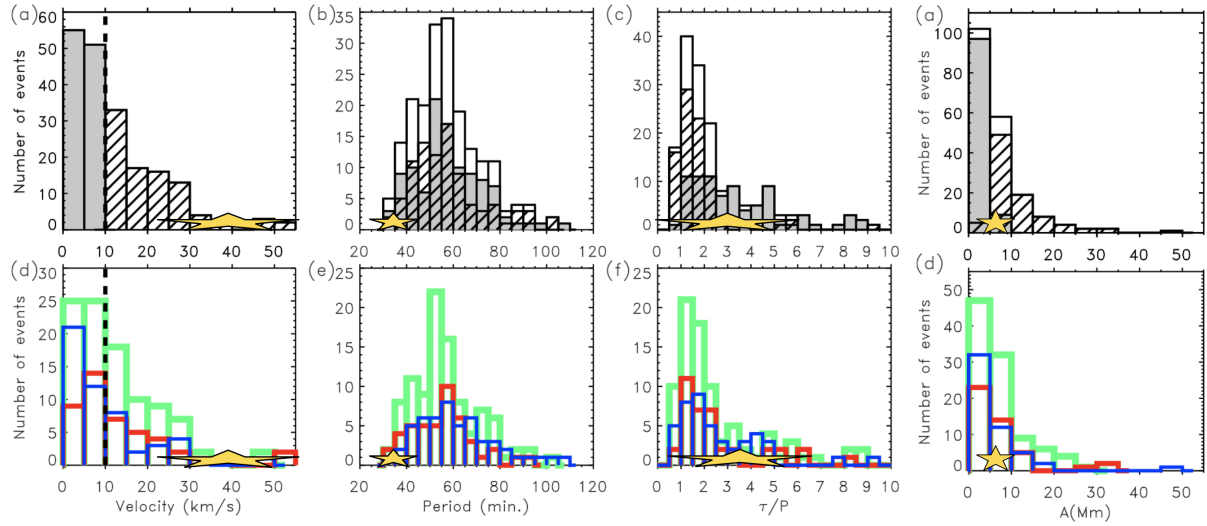


Figure 15: Comparison of obtained results with GONG catalog oscillations. The starred shapes represents the ranges of values obtained in the 2D simulation. Adapted from Figures 24 and 26 of Luna et al. 2018.

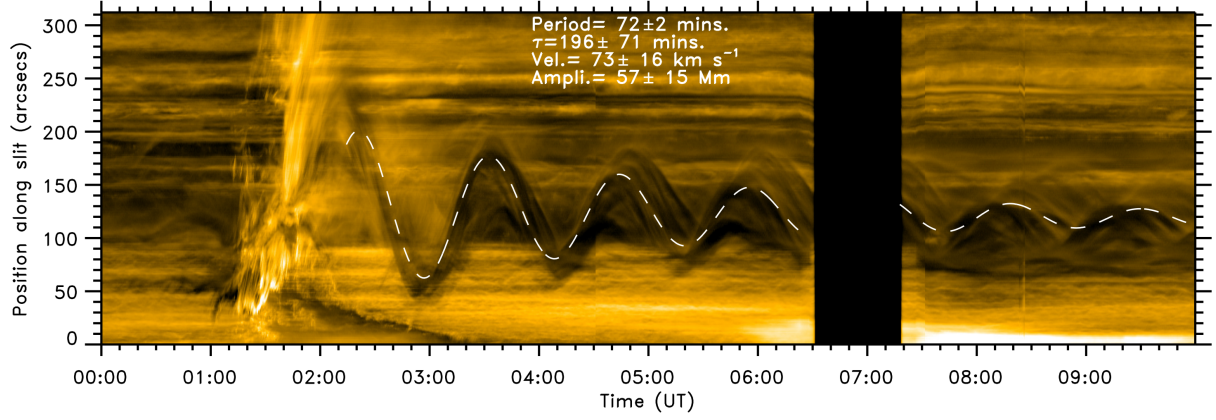


Figure 16: Adapted from Figure 8 of Luna et al. 2024. Time-distance diagram in AIA 171 Å of the prominence oscillations observed along a slit on March 15th. Bright structures between 01:10 and 02:10 UT corresponds to the impulsive phase when the oscillation is triggered.

4 Conclusions

In this work, we have developed a set of numerical simulations of increasing complexity to model the propagation of coronal shocks and their impact on prominences. The first group of numerical experiments consists of one-dimensional hydrodynamical shocks impacting a dense region that mimics a prominence. We concluded that the perturbation progressively transmits momentum to the dense object without modifying its total mass. This occurs through a series of shock and rarefaction waves that sweep the filament following the first impact by the initial shock. The filament gradually adapts its velocity to that of the surroundings until it moves with constant velocity equal to that of the initial post-shock medium while the initial shock propagates on the other side of the filament with the same characteristics it had at the beginning of the experiment. The second set of numerical experiments consists of one-dimensional simulations with thermal conduction and radiative cooling. In this case, the shock-like perturbation is generated by an explosive event caused by impulsive heating. Additionally, we have compared the asymptotic shock profiles obtained in simple numerical experiments with heat conduction to the analytical solutions for the shock jumps available in the early literature and found excellent agreement. In the second part of the Master’s Thesis, we performed a two-dimensional simulation in which a prominence is self-consistently formed through the evaporation-condensation process in the dips of a magnetic structure. The simulation includes thermal conduction, radiative losses, and heating. Shocks are generated by applying impulsive heating at the left footpoint of the magnetic structure, propagate along the curved magnetic field lines and impact the cool prominence mass. The impact of the shock on the prominence triggers oscillatory motions, resulting in Large Amplitude Longitudinal Oscillations (or LAOs) with parameters consistent with observational values. Moreover, the analysis confirms that the period of the oscillations is governed by the curvature of the supporting magnetic field lines, in agreement with the pendulum model.

Detailed studies of the propagation of realistic coronal shocks are scarce in the literature. The novel results obtained in this study provide a benchmark for the investigation of shocks in filament channel structures and, more generally, in the solar corona. As a global conclusion of this work, we have demonstrated that a coronal shock generated by a flare-like explosive event can trigger energetic prominence oscillations. The proposed model reproduces the observational results reported by Luna et al. 2024. We believe that many other observational cases, in which the trigger has not been identified, could also be explained by this model.

In this work, simplifications have been applied in the study of a flare impacting a prominence in the Sun. In three dimensions, more complex magnetic configurations could be considered. In addition, different impulsive heating profiles could be tested, and a parametric study of the resulting shocks and their impact on the prominence could be performed. Finally, generating synthetic images and comparing them with observations is necessary. However, all of these aspects are beyond the scope of the present Master’s Thesis.

A Unit handling with AMRVAC

The AMRVAC code assumes input values are written in *code units*, i.e. dimensionless values used directly for computing. The conversion into a physical system of units is achieved by setting three independent units like: length unit; mass or number density unit; temperature, time or velocity unit, from which all other magnitude units can be derived. The result simulations are independent of the system of units defined in the cases with no thermal conduction or viscosity, and they can be directly scaled to the desired system of units corresponding to the physical situation. Nevertheless, when thermal conduction or viscosity are considered, the spatial scale has an effect on the simulation output, making it dependent on the physical system.

The following example aims to illustrate the process. A set of three independent units are chosen for a simulation, namely:

- $L_C = 10^9$ cm for length,
- $\rho_C = 10^{-15}$ g cm $^{-3}$ for density,
- $T_C = 10^6$ K for temperature.

Then, any desired physical value u can be scaled to the dimensionless system simply dividing it by the reference unit u_C . Conversion of results in code units to the physical system of units can be performed after calculations are done. All of the different variable scaling values can be derived with the following relations:

$$n_C = \frac{\rho_C}{(1 + 4 X_{He}) m_H}, \quad (\text{A.1})$$

$$p_C = \frac{k_B}{\mu m_H} \rho_C T_C, \quad (\text{A.2})$$

$$V_C = \sqrt{p_C / \rho_C}, \quad (\text{A.3})$$

$$\tau_C = L_C / V_C, \quad (\text{A.4})$$

$$B_C = \sqrt{4\pi p_C}, \quad (\text{A.5})$$

where the scaling values are n_C for particle number density, p_C for pressure, V_C for velocity, τ_C for time and B_C for magnetic field. X_{He} is the Helium abundance, set as 0.1, m_H the mass of the Hydrogen atom in grams, k_B the Boltzmann constant in CGS and μ the mean molecular weight.

B Effect of the thermal conductivity on the shock profiles

The present Appendix contains the theoretical derivation followed to obtain the shock profiles for all variables out of the phase-diagram study performed by Lacey 1988. The study is performed for the 1D case, from a frame of reference at rest with the propagating perturbation; the incoming fluid is assumed to enter the domain through the left-hand side; the outgoing fluid is leaving the domain through the boundary on the right ($v > 0$). A scaled temperature, is defined as $\bar{T} = p/\rho = k_B T/\mu m_H$, with k_B Boltzmann constant, μ the mean molecular weight and m_H the mass of the Hydrogen atom. \bar{T} is the squared isothermal sound speed. A set of dimensionless variables are defined, normalized to the asymptotic pre-shock values, reached for $x \rightarrow -\infty$, which we label with the subindex 0.

$$\eta = v/v_0 , \quad (\text{B.1})$$

$$\rho = \rho_0/\eta = \rho_0 v_0/v , \quad (\text{B.2})$$

$$\tau = \bar{T}/v_0^2 = \eta(1 + \tau_0 - \eta) \left(= \frac{c_s^2}{\gamma} \frac{1}{v_0^2} = \frac{1}{\gamma M_0^2} \right) , \quad (\text{B.3})$$

$$\xi = x/l_0 , \quad (\text{B.4})$$

with l_0 a scale length that will be defined further down, and $\tau_0 = \bar{T}_0/v_0^2 = p_0/(\rho_0 v_0^2)$. Following the original article, the total dimensionless energy flux can be expressed as the sum of the advective and conductive fluxes:

$$f = g + q = 4\eta \left[\frac{5}{4}(1 + \tau_0) - \eta \right] - k(\tau) \frac{d\tau}{d\xi} , \quad (\text{B.5})$$

where $k(\tau) = \chi_\tau \tau^{5/2}$ is the dimensionless diffusion coefficient, defined by the dimensionless Spitzer coefficient and the dimensionless scaled temperature.

In the asymptotic pre-shock region ($\xi \rightarrow -\infty$) we will have $\eta = \eta_0 = 1$ and there will be no temperature gradient, so $d\tau/d\xi \rightarrow 0$ and the total energy flux becomes $f_0 = 1 + 5\tau_0$. As the total energy flux has to be conserved through space, $f = f_0$, and solving for $d\tau/d\xi$ and expressing it in terms of η , the following ordinary differential equation can be obtained:

$$\frac{d\eta}{d\xi} = \frac{(1 - \eta)[4\eta - (1 + 5\tau_0)]}{(1 + \tau_0 - 2\eta)k(\tau)} = \frac{(1 - \eta)[4\eta - (1 + 5\tau_0)]}{(1 + \tau_0 - 2\eta)\chi_\tau \eta^{5/2}(1 + \tau_0 - \eta)^{5/2}} . \quad (\text{B.6})$$

This equation depends only on dimensionless parameters. As the Spitzer coefficient is considered constant in space, the spatial variable can be redefined as $\xi' = \xi/\chi_\tau = x/(l_0 \chi_\tau)$; with that transformation, the resulting equation for ξ' does not depend at all on the characteristic physical values of the system under study:

$$\frac{d\eta}{d\xi'} = \frac{(1 - \eta)[4\eta - (1 + 5\tau_0)]}{(1 + \tau_0 - 2\eta)\eta^{5/2}(1 + \tau_0 - \eta)^{5/2}} . \quad (\text{B.7})$$

The actual solutions of these equations were not calculated by Lacey 1988: in his paper, he discussed their major physical properties but did not show the actual spatial profile for any of the variables. So, in the following we will carry out the numerical integration of the ODE to obtain the spatial profile of the dimensionless velocity $\eta(\xi')$, from which all other physical variables can be derived. There is a single parameter to vary, namely, τ_0 . Note that Eq. B.7 can be integrated analytically as well, but the analytical result is rather bulky and complicated, so, it is better to present here the numerically integrated solutions.

B.1 Solution of the ODE

The ODE (B.7) is numerically integrated with `solve_ivp` function from `scipy` module in Python, using an explicit Runge-Kutta method of fifth order. The solution will be studied in its dimensionless shape first, and then it will be dimensionalized and tested.

B.1.1 Dimensionless solution

The numerical solution of (B.7) provides $\eta(\xi')$ in the present situation where radiative cooling has been neglected. It is a monotonically decreasing function with space. The total energy flux can be equaled in the pre and post-shock regimes $f_0 = f_1$, which can be manipulated to obtain the post-shock value of the dimensionless velocity $\eta_1 = (1 + 5\tau_0)/4$. As the dimensionless scaled temperature can be related to the sonic Mach number (B.3), and this value has to be greater than 1 to have a shock, then $\tau_0 < 3/5$ has an upper limit, and $\eta_1 < 1$ as can be expected. The post-shock dimensionless scaled temperature can be determined as $\tau_1 = (1 + 5\tau_0)(3 - \tau_0)/16 > \tau_0$.

Now we will analyze the sign of the conduction flux q . As there is no radiative cooling, $d\tau/d\xi' \geq 0 \rightarrow q \leq 0$. Two different relations can be obtained from this limitation:

- From the total flux conservation $f = f_0 \rightarrow q \leq 0$ for $\eta_1 = (1 + 5\tau_0)/4 \leq \eta \leq \eta_0 = 1$.
- From the definition of q , the fact that $\eta(\xi')$ is monotonically decreasing and the definition of $\tau(\eta)$:

$$q = -k \frac{d\tau}{d\xi'} = -k \frac{d\tau}{d\eta} \frac{d\eta}{d\xi'} = -k(1 + \tau_0 - 2\eta) \frac{d\eta}{d\xi'} \leq 0, \quad (\text{B.8})$$

it can be deduced that $\eta \geq (1 + \tau_0) = \eta_2$ has to be fulfilled.

Figure 17a represents η_1 and η_2 with respect to τ_0 . Remembering that η begins at value 0 at $\xi' \rightarrow -\infty$ and decreases monotonically up to its final value, η_1 , it can be seen that when $\eta_2 > \eta_1$ there is a forbidden region in which the sign of q will not be well defined and η will experience a jump. The intersection point of this two lines happens for $\tau_0 = 1/3$, so there are two possible situations:

- $\tau_0 > 1/3$: $\eta_2 < \eta_1$ and the solution decreases smoothly until η_1 . All variables will be continuous.
- $\tau_0 < 1/3$: $\eta_2 > \eta_1$ and the solution decreases smoothly initially. The region (η_1, η_2) is forbidden so η will present a jump. It must also be taken into account that τ has to increase continuously from τ_0 to the maximum value τ_1 , which is fulfilled for both η_1 and $\eta_3 = (3 - \tau_0)/4$. For $\tau_0 < 1/3$, $\eta_3 > \eta_2$ and η will jump from η_3 to η_1 .

Figure 17b represents both q and τ with respect to η for the case $\tau_0 = 0.1 < 1/3$. The solution begins at $\eta_0 = 1$ and decreases monotonically in the region $q < 0$. It is seen that $\tau(\eta_3) = \tau(\eta_1)$ which will be the final dimensionless scaled temperature value. As τ increases monotonically and is continuous, η must jump from η_3 to η_1 , as marked by the black horizontal line.

It is concluded that the shock profile changes its shape due to thermal conduction. On the one hand, if the shock speed squared is smaller than three times the isothermal sound speed squared ($\tau_0 = p_0/\rho_0 \cdot 1/v_0^2 > 1/3$), there will be no jump in all variables, presenting a smooth shape. An example is shown in Figure 18a, showing both the different spatial profiles and the phase diagram $\tau - \eta$ equivalent to that of Figure 1a of Lacey 1988. On the other hand, if it is greater ($\tau_0 = p_0/\rho_0 \cdot 1/v_0^2 < 1/3$) the velocity profile (and consequently pressure and density) will present the jump discontinuity expected from shocks, but preceded by a smooth increase called *thermal precursor* while temperature will remain smooth. An example is shown in Figure 18b, including both the spatial profiles and the phase diagram $\tau - \eta$ equivalent to that of Figure 1c of Lacey 1988.

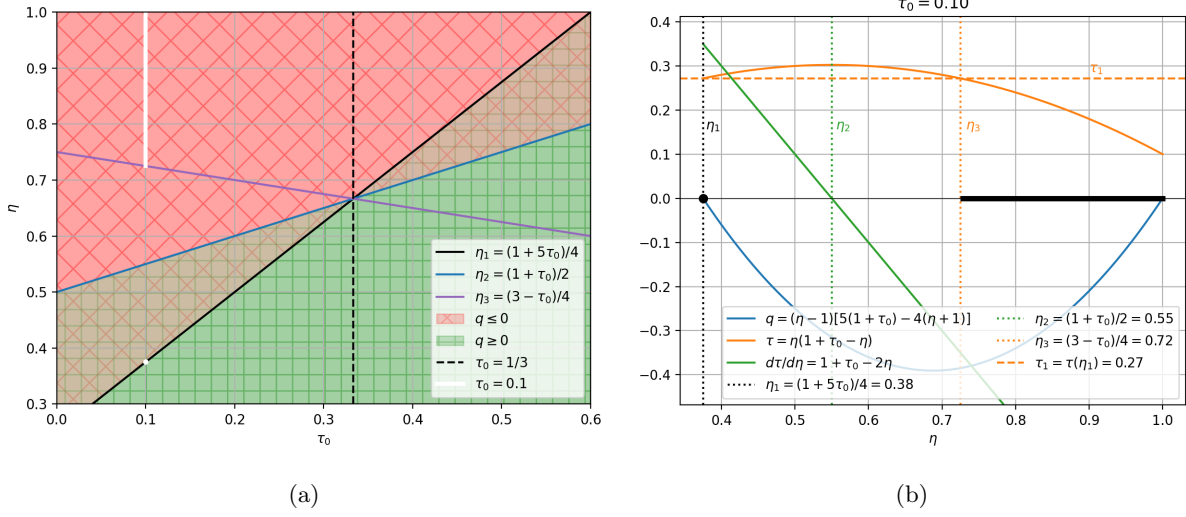


Figure 17: To the left, a map displaying η with respect to τ_0 and the sign of q . For a given value of τ_0 , the solution goes from $\eta_0 = 1$ and has to decrease monotonically to η_1 (black line). The conductive flux has to fulfill $q \leq 0$ so the region where $\eta_1 < \eta_2$ is not well defined. For $\tau_0 > 1/3$ this will not be a problem, but for $\tau_0 < 1/3$, η will jump from η_3 to η_1 . A vertical white line and point represents the possible values of η for $\tau_0 = 0.1$ displayed in the right panel.

The right panel represents q and τ with respect to η for the case $\tau_0 = 0.1$. As η decreases from $\eta_0 = 1$ to η_1 , τ reaches τ_1 at η_3 and has to remain constant. Then, η will jump from η_3 to η_1 , as shown by the black horizontal line. It can be seen that q is always negative.

The appearance of the thermal precursor seems to contradict the fact that the information propagation speed is limited to that of the sound speed in hydrodynamic fluids without thermal conduction or viscosity, so that nothing can propagate ahead of the shock front. Nevertheless, the inclusion of thermal conduction transforms the system of equations from hyperbolic to mixed hyperbolic-parabolic. In this new situation the information propagation speed is not limited and the existence of a thermal precursor ahead of the shock front is possible.

B.1.2 Dimensionalization of the solution

In this section we will explain how to transform the dimensionless solution $\eta(\xi')$ to the corresponding spatial profiles for the different physical values. The conversion of velocity, density, temperature and pressure is straightforward from their definition (B.1-B.3):

$$v = \eta \cdot v_0, \quad (B.9)$$

$$\rho = \rho_0/\eta, \quad (B.10)$$

$$T = \frac{\mu m_H}{k_B} v_0^2 \tau = \frac{\mu m_H}{k_B} v_0^2 \cdot \eta (1 + \tau_0 - \eta), \quad (B.11)$$

$$p = \frac{k_B}{\mu m_H} T \rho, \quad (B.12)$$

but they are still expressed with respect to the dimensionless spatial variable ξ' . As $\xi' = \xi/\chi_\tau = x/(l_0\chi_\tau) = x/L_0$, then the spatial scaling will be linear: $x = \xi' \cdot L_0$. This spatial scale will depend on the scale length and the Spitzer dimensionless coefficient, defined from the dimensionless conductive flux. In order to obtain it, the scaled diffusion coefficient $\bar{\kappa}(\bar{T})$ is defined:

$$Q = -\kappa(T) \frac{dT}{dx} = -\bar{\kappa}(\bar{T}) \frac{d\bar{T}}{dx}, \quad (B.13)$$

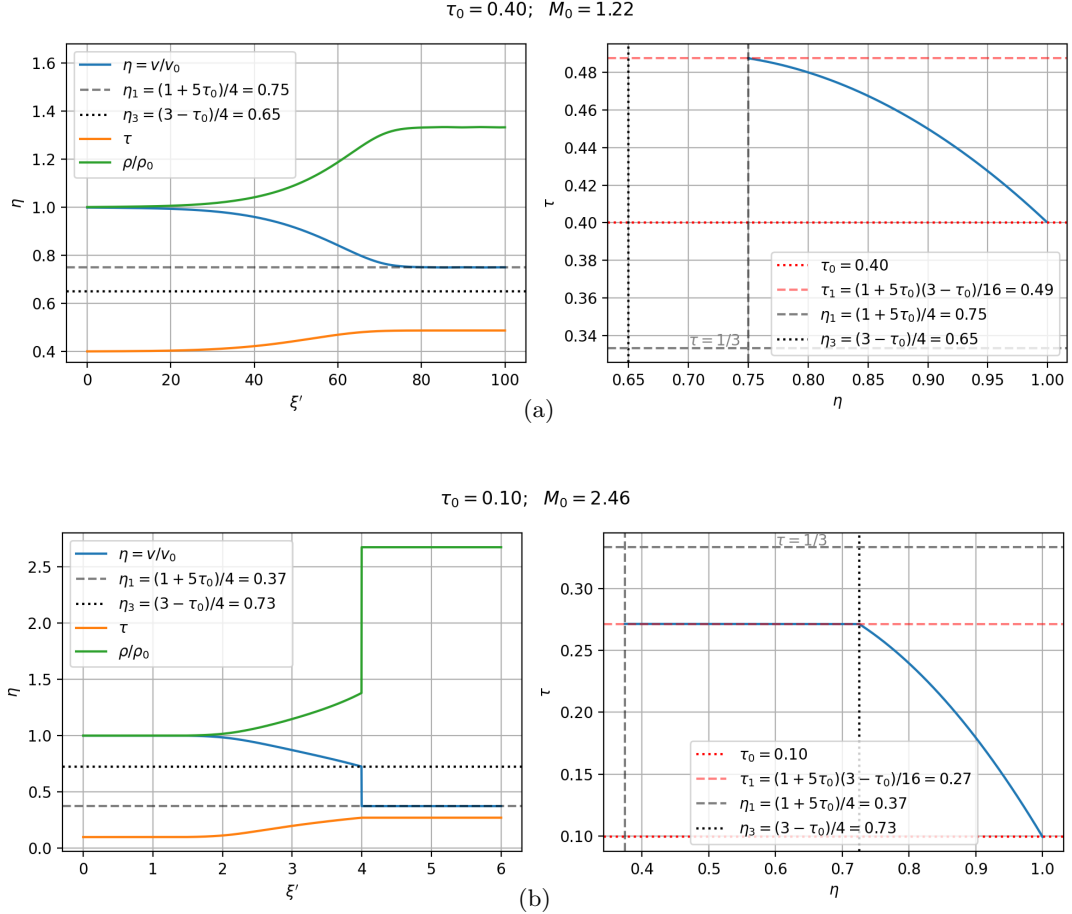


Figure 18: Spatial shock profiles of dimensionless variables and phase diagram of τ versus η for shocks under thermal conduction propagating to the left. 18a displays a case with $\tau_0 > 1/3$, with smooth profiles for all variables. 18b displays a case with $\tau_0 < 1/3$, with discontinuities in velocity and density profiles but a smooth profile for temperature.

with $\kappa(T) = \chi_T \cdot T^{5/2}$ the Spitzer diffusion coefficient and $\chi_T = 8 \cdot 10^{-7} \frac{\text{g}\cdot\text{cm}}{\text{K}^{7/2}\text{s}^3}$ the Spitzer diffusion coefficient used by AMRVAC, a typical value for coronal regions. From the definition of the scaled temperature it can be obtained that $\bar{\kappa} = (\mu m_H / k_B) \chi_T T^{5/2}$. To relate this scaled diffusion coefficient with the dimensionless diffusion coefficient the definition of the dimensionless conductive energy flux is used:

$$q = \frac{Q}{\frac{1}{2} \rho_0 v_0^3} = -\frac{\bar{\kappa} \frac{d\bar{T}}{dx}}{\frac{1}{2} \rho_0 v_0^3} = -k(\tau) \frac{d\tau}{d\xi}, \quad (\text{B.14})$$

and applying the relationship between $d\bar{T}/dx = v_0^2/l_0 \cdot d\tau/d\xi$, one can obtain:

$$k(\tau) = \frac{2\bar{\kappa}(\bar{T})}{\rho_0 l_0 v_0} = \chi_\tau \tau^{5/2}, \quad (\text{B.15})$$

which finally relates the dimensional and dimensionless Spitzer coefficients χ_T , χ_τ , through the relation:

$$L_0 = l_0 \chi_\tau = \frac{2v_0^4}{\rho_0} \left(\frac{\mu m_H}{k_B} \right)^{7/2} \chi_T. \quad (\text{B.16})$$

The spatial extension of the thermal precursor will increase considerably with the shock propagation speed and decrease with the density of the pre-shock medium.

B.1.3 Jump relations

Through the manipulation of the previous equations the theoretical jumps expected can be derived:

$$\frac{T_1}{T_0} = \frac{\tau_1}{\tau_0} = \frac{(1 + 5\tau_0)(3 - \tau_0)}{16\tau_0} \quad (\text{B.17})$$

$$\frac{\rho_1}{\rho_0} = \frac{\eta_0}{\eta_1} = 1/\eta_1 = \frac{4}{1 + 5\tau_0} \quad (\text{B.18})$$

$$\frac{p_1}{p_0} = \frac{\tau_1/\eta_1}{\tau_0/\eta_0} = \frac{3 - \tau_0}{4\tau_0} \quad (\text{B.19})$$

$$\frac{v_1}{v_0} = \frac{\eta_1}{\eta_0} = \eta_1 = \frac{1 + 5\tau_0}{4} \quad (\text{B.20})$$

These expressions are used to calculate the values of Table 2.

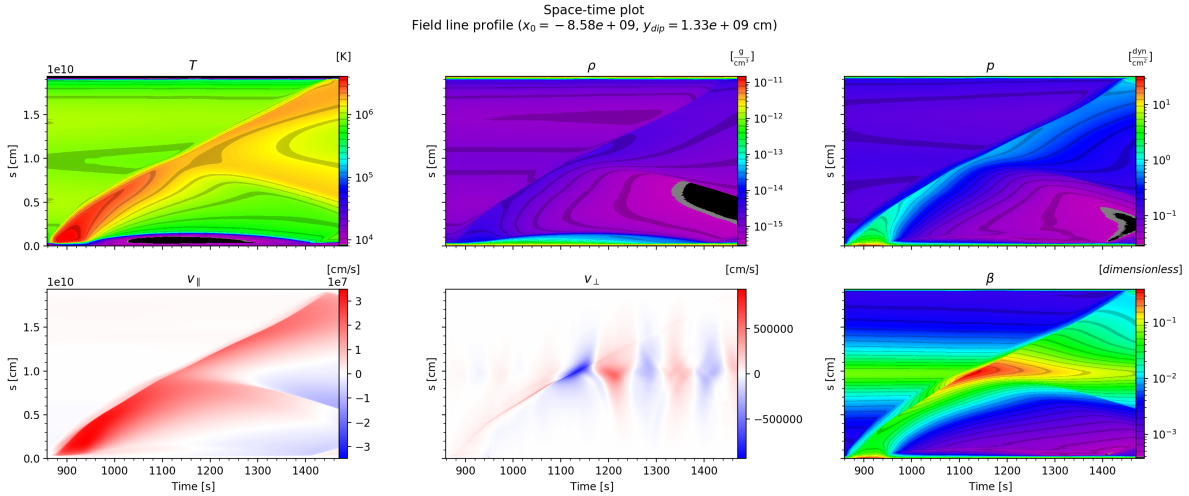


Figure 19: Space-time maps for perturbation generation and propagation. There is no prominence around $s = 10^{10}$ cm as in Figure 11, so the path covered by the shock is twice as long and much more homogeneous.

C Thermal conduction in 2D coronal shocks

The two-dimensional numerical simulation of Section 3 proved that the shock-like perturbation generated is not accurately described by the theory about shock profiles affected by thermal conduction developed by Lacey 1988 and explained in Appendix B. The observed jumps do not match precisely the theoretical jumps nor the ideal hydrodynamic jumps. In this Appendix we will prove that this is due to the short inhomogeneous path covered by the perturbation until they impact the prominence, without enough time to acquire its natural shape. To do so, a new test is developed with the same set-up of Section 3 but reducing the background heating so that evaporation is decreased. Not enough time is given for the condensation of the prominence mass in the dip of the field lines, so when activating the impulsive heating, the generated perturbation will propagate through a much more homogeneous medium.

Figure 19 shows the space-time maps for the generation and propagation of the perturbation along the field line centered at the impulsive heating maximum. It can be appreciated that the path traveled by the perturbation doubles the length of Figure 11 because there is no prominence to impact at $s \approx 10^{10}$ cm, and is much more homogeneous. There is still a slight over-density in the dipped region of the field line due to accumulation of plasma from the relaxation of the initial conditions. This situation is closer to the ideal circumstances considered by Lacey 1988, so a fit to the theoretical profiles will be performed. Figure 20 shows the evolution of the position of the shock front and its instantaneous propagation velocity. This can be used to calculate the parameter τ_0 at different moments of time, allowing to compute the theoretical profiles. It can be seen that the perturbation slows down until $t = 1100$ s, time at which it reaches the dipped region of the field line and then maintains a steady velocity.

The last phase of propagation at constant speed will be compared with the theoretical expected results, as shown in Figure 21. The shock profile is drawn in the upper plots in olive-green color. The theoretical thermal conduction profile obtained with the pre-shock values and the instantaneous propagation speed is over-plotted in orange dashed lines. The relative difference between both profiles is shown in the bottom panels, zoomed to the spatial region defined by the vertical dotted lines. The similarity between both profiles is significant, allowing to validate that shock-like perturbations affected by thermal conduction in a low β plasma propagate along the field lines like they would in a one-dimensional homogeneous situation with no magnetic field.

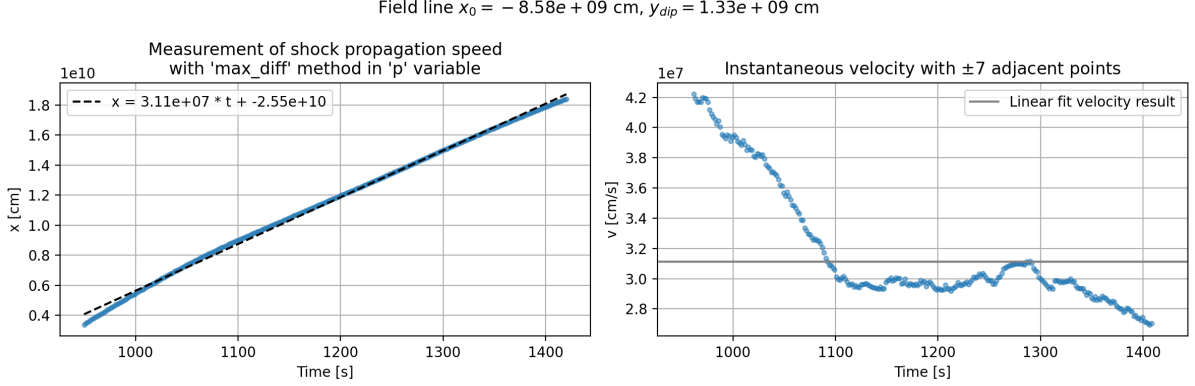


Figure 20: Detection of shock front position and instantaneous propagation velocity along the field line centered at the impulsive heating maximum.

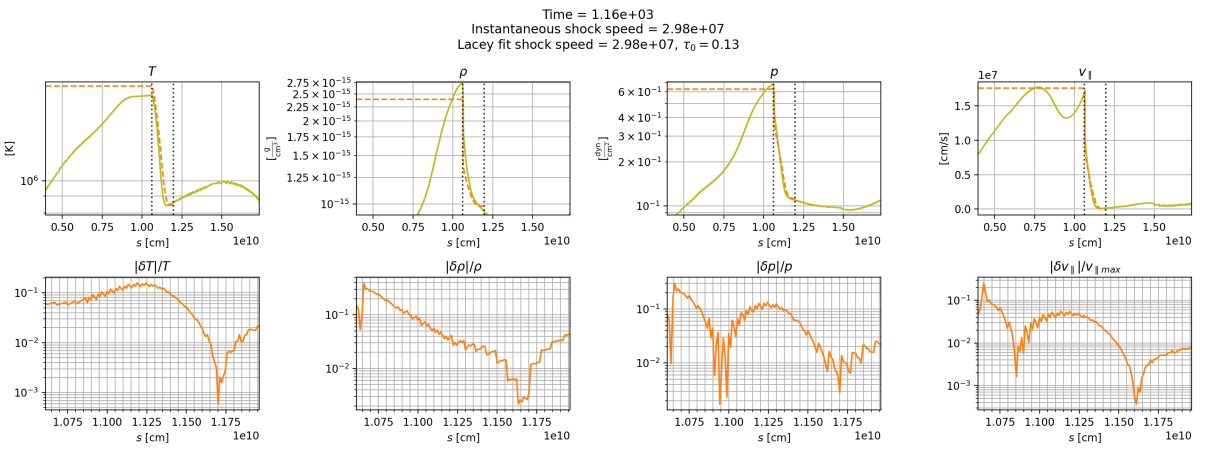


Figure 21: Shock profiles for the field line centered at the impulsive heating maximum. Top panels display the comparison among the obtained shock profile (olive-green line) and the theoretically expected result (orange line). Bottom panels display the relative error obtained for each line. The vertical dotted lines of the upper panels define the spatial region zoomed in the bottom panels.

References

- Antiochos, SK and Klimchuk, JA (1991). “A model for the formation of solar prominences”. In: *The Astrophysical Journal* 378. Publisher: IOP Publishing, p. 372. DOI: [10.1086/170437](https://doi.org/10.1086/170437). URL: <http://adsabs.harvard.edu/doi/10.1086/170437>.
- Arregui, I, Oliver, R, and Ballester, JL (2018). “Prominence oscillations”. In: *Living Reviews in Solar Physics* 15.1, 3, p. 3. DOI: [10.1007/s41116-018-0012-6](https://doi.org/10.1007/s41116-018-0012-6).
- Benz, AO (2008). “Flare Observations”. In: *Living Reviews in Solar Physics* 5.1. Publisher: Springer International Publishing, p. 1. DOI: [10.12942/lrsp-2008-1](https://doi.org/10.12942/lrsp-2008-1). URL: http://adsabs.harvard.edu/cgi-bin/nph-data_query?bibcode=2008LRSP....5....1B&link_type=EJOURNAL.
- Chen, J et al. (2017). “A reexamination of a filament oscillation event on 2013 March 15”. In: *Astrophysics and Space* ... URL: http://adsabs.harvard.edu/cgi-bin/nph-data_query?bibcode=2017Ap%26SS.362..165C&link_type=EJOURNAL.
- Colgan, J et al. (2008). “Radiative Losses of Solar Coronal Plasmas”. In: *The Astrophysical Journal* 689.1, pp. 585–592. DOI: [10.1086/592561](https://doi.org/10.1086/592561).
- Felipe, T, Khomenko, E, and Collados, M (2010). “Magneto-acoustic Waves in Sunspots: First Results From a New Three-dimensional Nonlinear Magnetohydrodynamic Code”. In: *The Astrophysical Journal* 719.1, pp. 357–377. DOI: [10.1088/0004-637X/719/1/357](https://doi.org/10.1088/0004-637X/719/1/357). arXiv: [1006.2998 \[astro-ph.SR\]](https://arxiv.org/abs/1006.2998).
- Gudiksen, BV et al. (2011). “The stellar atmosphere simulation code Bifrost. Code description and validation”. In: *A&A* 531, A154, A154. DOI: [10.1051/0004-6361/201116520](https://doi.org/10.1051/0004-6361/201116520). arXiv: [1105.6306 \[astro-ph.SR\]](https://arxiv.org/abs/1105.6306).
- Hyder, CL (1966). “Winking Filaments and Prominence and Coronal Magnetic Fields”. In: *Zeitschrift für Astrophysik* 63, p. 78. URL: http://adsabs.harvard.edu/cgi-bin/nph-data_query?bibcode=1966ZA....63...78H&link_type=GIF.
- Jerčić, V, Keppens, R, and Zhou, Y (2022). “Multi-threaded prominence oscillations triggered by a coronal shock wave”. In: *A&A* 658, A58, A58. DOI: [10.1051/0004-6361/202142127](https://doi.org/10.1051/0004-6361/202142127). arXiv: [2111.09019 \[astro-ph.SR\]](https://arxiv.org/abs/2111.09019).
- Karpen, JT, Tanner, SEM, Antiochos, SK, and DeVore, CR (2005). “Prominence Formation by Thermal Nonequilibrium in the Sheared-Arcade Model”. In: *The Astrophysical Journal* 635.2. Publisher: IOP Publishing, pp. 1319–1328. DOI: [10.1086/497531](https://doi.org/10.1086/497531). URL: http://adsabs.harvard.edu/cgi-bin/nph-data_query?bibcode=2005ApJ...635.1319K&link_type=ABSTRACT.
- Keppens, R and Xia, C (2014). “The Dynamics of Funnel Prominences”. In: *The Astrophysical Journal* 789.1. Publisher: IOP Publishing, p. 22. DOI: [10.1088/0004-637X/789/1/22](https://doi.org/10.1088/0004-637X/789/1/22). URL: http://adsabs.harvard.edu/cgi-bin/nph-data_query?bibcode=2014ApJ...789...22K&link_type=ABSTRACT.
- Keppens, R et al. (2023). “MPI-AMRVAC 3.0: Updates to an open-source simulation framework”. In: *A&A* 673, A66. DOI: [10.1051/0004-6361/202245359](https://doi.org/10.1051/0004-6361/202245359). URL: <https://doi.org/10.1051/0004-6361/202245359>.
- Klecze, J and Kuperus, M (1969). “Oscillatory Phenomena in Quiescent Prominences”. In: *Solar Physics* 6.1. Publisher: Springer Netherlands, pp. 72–79. DOI: [10.1007/BF00146797](https://doi.org/10.1007/BF00146797). URL: http://adsabs.harvard.edu/cgi-bin/nph-data_query?bibcode=1969SoPh....6....72K&link_type=ABSTRACT.
- Lacey, CG (1988). “The Structure of Shocks with Thermal Conduction and Radiative Cooling”. In: *The Astrophysical Journal* 326, p. 769. DOI: [10.1086/166136](https://doi.org/10.1086/166136).
- Liakh, V, Luna, M, and Khomenko, E (2021). “Large-amplitude longitudinal oscillations in solar prominences simulated with different resolutions”. In: *Astronomy & Astrophysics* 654. Publisher: EDP Sciences, A145. ISSN: 0004-6361, 1432-0746. DOI: [10.1051/0004-6361/202141524](https://doi.org/10.1051/0004-6361/202141524). URL: <https://www.aanda.org/articles/aa/abs/2021/10/aa41524-21/aa41524-21.html> (visited on 05/05/2022).

- Liakh, V, Luna, M, and Khomenko, E (2020). “Numerical simulations of large-amplitude oscillations in flux rope solar prominences”. In: *A&A* 637, A75, A75. doi: [10.1051/0004-6361/201937083](https://doi.org/10.1051/0004-6361/201937083). arXiv: [2003.04343 \[astro-ph.SR\]](https://arxiv.org/abs/2003.04343).
- (2023). “Numerical simulations of prominence oscillations triggered by external perturbations”. In: *A&A* 673, A154, A154. doi: [10.1051/0004-6361/202245765](https://doi.org/10.1051/0004-6361/202245765). arXiv: [2303.15348 \[astro-ph.SR\]](https://arxiv.org/abs/2303.15348).
- Long, DM et al. (2017). “Understanding the Physical Nature of Coronal “EIT Waves””. In: *Springer Solar Physics* 292.1, 7, p. 7. doi: [10.1007/s11207-016-1030-y](https://doi.org/10.1007/s11207-016-1030-y). arXiv: [1611.05505 \[astro-ph.SR\]](https://arxiv.org/abs/1611.05505).
- Luna, M, Díaz, AJ, and Karpen, J (2012a). “The Effects of Magnetic-field Geometry on Longitudinal Oscillations of Solar Prominences”. In: *The Astrophysical Journal* 757.1, p. 98. doi: [10.1088/0004-637X/757/1/98](https://doi.org/10.1088/0004-637X/757/1/98). URL: <https://dx.doi.org/10.1088/0004-637X/757/1/98>.
- Luna, M and Karpen, J (2012). “Large-amplitude Longitudinal Oscillations in a Solar Filament”. In: *The Astrophysical Journal* 750.1, L1, p. L1. doi: [10.1088/2041-8205/750/1/L1](https://doi.org/10.1088/2041-8205/750/1/L1). arXiv: [1203.5027 \[astro-ph.SR\]](https://arxiv.org/abs/1203.5027).
- Luna, M, Karpen, JT, and Devore, CR (2012b). “Formation and Evolution of a Multi-threaded Solar Prominence”. In: *The Astrophysical Journal* 746.1. Publisher: IOP Publishing, p. 30. doi: [10.1088/0004-637X/746/1/30](https://doi.org/10.1088/0004-637X/746/1/30). URL: http://adsabs.harvard.edu/cgi-bin/nph-data_query?bibcode=2012ApJ...746...30L&link_type=ABSTRACT.
- Luna, M et al. (2018). “GONG Catalog of Solar Filament Oscillations Near Solar Maximum”. In: *The Astrophysical Journal Supplement Series* 236.2, p. 35. doi: [10.3847/1538-4365/aabde7](https://doi.org/10.3847/1538-4365/aabde7). URL: <https://dx.doi.org/10.3847/1538-4365/aabde7>.
- Luna, M et al. (2016). “On the Robustness of the Pendulum Model for Large-amplitude Longitudinal Oscillations in Prominences”. In: *The Astrophysical Journal* 817.2, 157, p. 157. doi: [10.3847/0004-637X/817/2/157](https://doi.org/10.3847/0004-637X/817/2/157). arXiv: [1512.05125 \[astro-ph.SR\]](https://arxiv.org/abs/1512.05125).
- Luna, M and Moreno-Insertis, F (2021). “Large-amplitude Prominence Oscillations following Impact by a Coronal Jet”. In: *The Astrophysical Journal* 912.1, p. 75. doi: [10.3847/1538-4357/abec46](https://doi.org/10.3847/1538-4357/abec46). URL: <https://dx.doi.org/10.3847/1538-4357/abec46>.
- Luna, M et al. (2024). “Study of the excitation of large-amplitude oscillations in a prominence by nearby flares”. en. In: *Astronomy & Astrophysics* 691, A354. ISSN: 0004-6361, 1432-0746. doi: [10.1051/0004-6361/202450869](https://doi.org/10.1051/0004-6361/202450869). URL: <https://www.aanda.org/10.1051/0004-6361/202450869> (visited on 11/26/2024).
- Mackay, DH et al. (2010). “Physics of Solar Prominences: II—Magnetic Structure and Dynamics”. In: *Space Science Reviews* 151.4, pp. 333–399. doi: [10.1007/s11214-010-9628-0](https://doi.org/10.1007/s11214-010-9628-0). arXiv: [1001.1635 \[astro-ph.SR\]](https://arxiv.org/abs/1001.1635).
- Ni, YW et al. (2022). “Decayless longitudinal oscillations of a solar filament maintained by quasi-periodic jets”. en. In: *Astronomy & Astrophysics* 663. Publisher: EDP Sciences, A31. ISSN: 0004-6361, 1432-0746. doi: [10.1051/0004-6361/202142979](https://doi.org/10.1051/0004-6361/202142979). URL: <https://www.aanda.org/articles/aa/abs/2022/07/aa42979-21/aa42979-21.html> (visited on 02/27/2023).
- Parenti, S (2014). “Solar Prominences: Observations”. In: *Living Reviews in Solar Physics* 11.1, p. 1. doi: [10.12942/lrsp-2014-1](https://doi.org/10.12942/lrsp-2014-1). URL: <https://doi.org/10.12942/lrsp-2014-1>.
- Priest, E (2014). *Magnetohydrodynamics of the Sun*. Cambridge University Press. ISBN: 9780521854719. doi: [10.1017/CBO9781139020732](https://doi.org/10.1017/CBO9781139020732).
- Rempel, M (2017). “Extension of the MURaM Radiative MHD Code for Coronal Simulations”. In: *The Astrophysical Journal* 834.1, 10, p. 10. doi: [10.3847/1538-4357/834/1/10](https://doi.org/10.3847/1538-4357/834/1/10). arXiv: [1609.09818 \[astro-ph.SR\]](https://arxiv.org/abs/1609.09818).
- Spitzer, L (1962). “Physics of fully ionized gases, 2nd edition”. In: *Physics of fully ionized gases, 2nd edition*. New York: Interscience.

- Terradas, J et al. (2013). "Magnetohydrodynamic Waves in Two-dimensional Prominences Embedded in Coronal Arcades". In: *The Astrophysical Journal* 778.1. Publisher: IOP Publishing, p. 49. DOI: [10.1088/0004-637X/778/1/49](https://doi.org/10.1088/0004-637X/778/1/49). URL: http://adsabs.harvard.edu/cgi-bin/nph-data_query?bibcode=2013ApJ...778...49T&link_type=ABSTRACT.
- Toro, EF (2009). "The Riemann Problem for the Euler Equations". In: *Riemann Solvers and Numerical Methods for Fluid Dynamics: A Practical Introduction*. Berlin, Heidelberg: Springer Berlin Heidelberg, pp. 115–162. ISBN: 978-3-540-49834-6. DOI: [10.1007/b79761_4](https://doi.org/10.1007/b79761_4). URL: https://doi.org/10.1007/b79761_4.
- Turk, MJ et al. (2011). "yt: A Multi-code Analysis Toolkit for Astrophysical Simulation Data". In: *The Astrophysical Journal* 192.1, 9, p. 9. DOI: [10.1088/0067-0049/192/1/9](https://doi.org/10.1088/0067-0049/192/1/9). arXiv: [1011.3514 \[astro-ph.IM\]](https://arxiv.org/abs/1011.3514).
- Vögler, A et al. (2005). "Simulations of magneto-convection in the solar photosphere. Equations, methods, and results of the MURAM code". In: *A&A* 429, pp. 335–351. DOI: [10.1051/0004-6361:20041507](https://doi.org/10.1051/0004-6361:20041507).
- Xia, C, Chen, PF, and Keppens, R (2012). "SIMULATIONS OF PROMINENCE FORMATION IN THE MAGNETIZED SOLAR CORONA BY CHROMOSPHERIC HEATING". In: *The Astrophysical Journal Letters* 748.2, p. L26. DOI: [10.1088/2041-8205/748/2/L26](https://doi.org/10.1088/2041-8205/748/2/L26). URL: <https://dx.doi.org/10.1088/2041-8205/748/2/L26>.
- Zel'dovich, YB and Raizer, YP (1967). *Physics of shock waves and high-temperature hydrodynamic phenomena*. Elsevier.
- Zhang, LY, Fang, C, and Chen, PF (2019). "Damping Mechanisms of the Solar Filament Longitudinal Oscillations in the Weak Magnetic Field". en. In: *The Astrophysical Journal* 884.1. Publisher: American Astronomical Society, p. 74. ISSN: 0004-637X. DOI: [10.3847/1538-4357/ab3d3a](https://doi.org/10.3847/1538-4357/ab3d3a). URL: <https://doi.org/10.3847%2F1538-4357%2Fab3d3a> (visited on 10/10/2020).
- Zhang, QM, Chen, PF, Xia, C, and Keppens, R (2012). "Observations and simulations of longitudinal oscillations of an active region prominence". en. In: *Astronomy & Astrophysics* 542. Publisher: EDP Sciences, A52. ISSN: 0004-6361, 1432-0746. DOI: [10.1051/0004-6361/201218786](https://doi.org/10.1051/0004-6361/201218786). URL: <https://www.aanda.org/articles/aa/abs/2012/06/aa18786-12/aa18786-12.html> (visited on 10/19/2020).
- Zhang, QM et al. (2013). "Parametric survey of longitudinal prominence oscillation simulations". In: *Astronomy and Astrophysics* 554. Publisher: EDP Sciences, p. 124. DOI: [10.1051/0004-6361/201220705](https://doi.org/10.1051/0004-6361/201220705). URL: http://adsabs.harvard.edu/cgi-bin/nph-data_query?bibcode=2013A%26A...554A.124Z&link_type=ABSTRACT.
- Zhou, YH et al. (2018). "Three-dimensional MHD Simulations of Solar Prominence Oscillations in a Magnetic Flux Rope". In: *The Astrophysical Journal* 856.2. Publisher: IOP Publishing, p. 179. DOI: [10.3847/1538-4357/aab614](https://doi.org/10.3847/1538-4357/aab614). URL: <http://stacks.iop.org/0004-637X/856/i=2/a=179?key=crossref.8d45f0c8322c0e1a7e7607cc4e27a562>.
- Zhou, Y, Li, X, Hong, J, and Keppens, R (2023). "Winking filaments due to cyclic evaporation-condensation". en. In: *Astronomy & Astrophysics* 675, A31. ISSN: 0004-6361, 1432-0746. DOI: [10.1051/0004-6361/202346004](https://doi.org/10.1051/0004-6361/202346004). URL: <https://www.aanda.org/10.1051/0004-6361/202346004> (visited on 06/11/2025).